AD_____

Award Number: W81XWH-09-1-0502

TITLE: Breast Cancer-Targeted Nuclear Drug Delivery Overcoming Drug Resistance for Breast Cancer Chemotherapy

PRINCIPAL INVESTIGATOR: Maciej Radosz

CONTRACTING ORGANIZATION: University of Wyoming
Laramie, WY 82071

REPORT DATE: September 2012

TYPE OF REPORT: Annual

PREPARED FOR: U.S. Army Medical Research and Materiel Command
Fort Detrick, Maryland 21702-5012

REPORT DOCUMENTATION PAGE

Form Approved
OMB No. 0704-0188

1. REPORT DATE	2. REPORT TYPE	3. DATES COVERED
September 2012	Annual	1 September 2011 – 31 August 2012

4. TITLE AND SUBTITLE

Breast Cancer-Targeted Nuclear Drug Delivery Overcoming Drug Resistance for Breast Cancer Chemotherapy

5a. CONTRACT NUMBER

5b. GRANT NUMBER
W81XWH-09-1-0502

5c. PROGRAM ELEMENT NUMBER

6. AUTHOR(S)

Maciej Radosz
Youqing Shen

E-Mail: Radosz@uwyo.edu

5d. PROJECT NUMBER

5e. TASK NUMBER

5f. WORK UNIT NUMBER

7. PERFORMING ORGANIZATION NAME(S) AND ADDRESS(ES)

University of Wyoming
Laramie, WY 82071

8. PERFORMING ORGANIZATION REPORT NUMBER

9. SPONSORING / MONITORING AGENCY NAME(S) AND ADDRESS(ES)
U.S. Army Medical Research and Materiel Command
Fort Detrick, Maryland 21702-5012

10. SPONSOR/MONITOR'S ACRONYM(S)

11. SPONSOR/MONITOR'S REPORT NUMBER(S)

12. DISTRIBUTION / AVAILABILITY STATEMENT
Approved for Public Release; Distribution Unlimited

13. SUPPLEMENTARY NOTES

14. ABSTRACT

Due to the cell membrane-associated and intracellular drug resistance mechanisms, the depleted cytoplasmic drug concentration allows breast cancer cells to survive and resist chemotherapeutic regiments. Therefore, the goal of this proposal is to develop targeted charge-reversal nanoparticles (TCRNs) to overcome breast cancer drug resistance. We finished the task 1 and 2. A series of TCRNs were synthesized and characterized, including a charge-reversal polymer, a charge-reversal liposome and a charge-reversal peptide. Such TCRNs effectively enhance the cellular uptake of the nanoparticles and exhibit higher cytotoxicity to cancer cells, showing a great promise for in vivo applications. Moreover, a series of degradable dendrimers and its applications in delivering anticancer drugs were developed as novel targeted delivery systems. In addition, a new nanorod-like nanocarriers was prepared and demonstrated be advantageous over similar spherical nanocarriers in targeting cancer cells.

15. SUBJECT TERMS
Nuclear Drug Delivery

16. SECURITY CLASSIFICATION OF:			17. LIMITATION OF ABSTRACT	18. NUMBER OF PAGES	19a. NAME OF RESPONSIBLE PERSON
a. REPORT	b. ABSTRACT	c. THIS PAGE			USAMRMC
U	U	U	UU	52	19b. TELEPHONE NUMBER *(include area code)*

Table of Contents

Introduction

We worked according to the TASK 1 and 2 in the SOW:

STATEMENT OF WORK

Breast Cancer-Targeted Nuclear Drug Delivery Overcoming Drug Resistance for Breast Cancer Chemotherapy
University of Wyoming, 1000 E Univ Ave, Laramie, Wyoming

Maciej Radosz (PI)
Youqing Shen, Ph.D. (Co-PI)
William J. Murdoch, Ph.D. (Co-PI)

TASK 1. To synthesize and optimize folic-acid– or LHRH-functionalized charge reversal nanoparticles (12 Months):

a. Synthesize linear polyethyleneimine (PEI, Mn ~0.8-10kDa) by ring-opening polymerization.
b. React the PEI with proper 5-membered ring-anhydrides to prepare charge-reversal PEIs (PEI/amides), characterize and optimize their charge-reversal kinetics.
c. Introduce folic acid or LHRH to the PEI/amides using a post-reaction method.
d. Fabricate and characterize TCRNs.
e. Load drugs doxorubicin (DOX), camptothecin (CPT) and other drugs for breast cancer to TCRNs.

Milestone 1: To obtain the FA- and LHRH-functionalized TCRNs with optimal charge-reversal kinetics, targeting group density, size, and drug loading.

TASK 2. To in vitro evaluate the TCRNs for breast cancer chemotherapy (12 Months):

a. In vitro test drug release profile at pH 7.4.
b. Test stability in blood.
c. In vitro test cellular binding (competitive inhibition method).
d. In vitro test cellular uptake of TCRNs (flow cytometry, confocal laser-light scanning fluorescence microscopy).
e. Intracellular trafficking.
f. In vitro cytotoxicity to breast cancer cells.

Milestone 2: To screen out the TCRNs with the highest in vitro anti-breast cancer activity.

TASK 3. To in vivo evaluate TCRNs' anti-breast cancer efficacy (12 months)

a. In vivo test biodistribution and tumor targeting efficiency using nude mice (about 120 mice).
b. In vivo test and compare anticancer activity using nude mice with ip tumors and sc tumors treated by ip and iv injections (about 200 mice).

Milestone 3: To screen out the TCRNs with the highest in vivo anticancer activity

Body

Previously we prepared amidized PolyHis^{-s} as the charge-reversal polymer and demonstrated it was water-soluble and negatively charged at the neutral pH but converted back to PolyHis having strong lysosomal lysis ability at lysosomal pH. Therefore, the PolyHis^{-s} was considered as a promising breast-cancer-targeted nuclear drug delivery carrier.

During the year, we continued focusing on the development of a charge-reversal liposome and a charge-reversal peptide as nuclear-targeted drug carriers. Moreover, we synthesized a series of degradable dendrimers and applied such dendrimers to formulate novel drug delivery systems. In addition, a new nanorod-like nanocarriers was prepared and demonstrated be advanced to similar spherical nanocarriers. Besides, we reviewed the current achievements as well as proposed new criterions and strategies of translational nanocarriers for cancer chemotherapy.

1. Nuclear drug delivery by charge-reversal carriers

1.1 Nuclear drug delivery by a charge-reversal liposome

Liposomes have been extensively investigated as nano-sized carriers for targeted cancer drug delivery because they could easily extravasate from the tumor's leaky blood capillaries and preferentially deliver drugs to tumor tissues via the enhanced permeability and retention (EPR) effect[1, 2]. Cationic liposomes could be fast internalized by cancer cells; however, they could also induce the systematic toxicity[3, 4] and fast blood clearance[5, 6], limiting their applications *in vivo*. Although PEGylation is a widely used approach to shield their positively-charged surfaces and thereby prolong their blood circulation time[7, 8], it reduces the interactions of modified liposomes with cells and thus resulting in the significant hindering of the fast cellular uptake.

Herein, we prepared a cationic dioctadecyl lipid with oligoethyleneimine (DOLPEI) (Scheme 1). The DOLPEI had a intrinsic biocompatibility due to the introduction of dioctadecyl groups as the hydrophobic tails[9]. The linear ethyleneimine oligomer (LPEI) chain with only 11 repeating units played the role of hydrophilic head group of the lipid to increase the ability of crossing the cell membrane. We amidized the amines in the LPEI chain with β-carboxylic acid amides (DOLPEI/amide) to make the formulated DOLPEI/amide liposome negatively charged at the physiological pH. Once it located inside the cancer cells' lysosomes at lower pH, the

amides could be quickly hydrolyzed and convert to amines, regenerating the positively charged liposomes to escape from the lysosomes and traverse to the nuclei, where the encapsulated anti-cancer drugs were released.

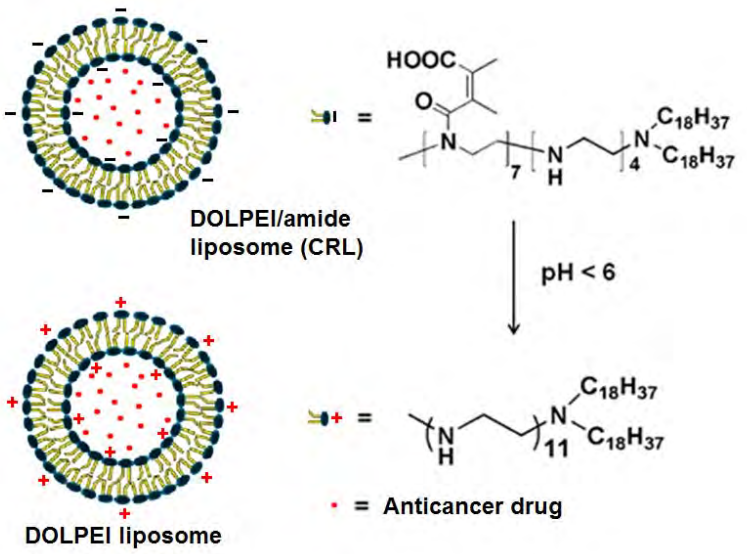

Scheme 1. The structure of the charge-reversal liposome (CRL) and its pH-triggered charge reversal.

1.1.1 Synthesis of the DOLPEI/amide

As showed in Scheme 2, we firstly prepared the dioctadecylamino polyMeOz (DOPMeOz) via living cationic polymerization of 2-methyl-2-oxazoline (MeOz) terminated with dioctadecylamine[10] and determined the structure via ^{1}HNMR (Figure 1a). The resulting DOPMeOz was hydrolyzed in 10% hydrochloride solution and produced DOLEPI after adjusting the reaction solution pH higher than 11. The amines in the LPEI were amidized by an anhydride 2,3-dimethylmaleic anhydride (DM) in water at pH 8.5 as reported[11]. The resulting dioctadecyl polyethylene amides (DOLPEI/amide) were stable in the basic environment (pH > 8.5). Approximately 66.1% of the secondary amine was amidized was determined by ^{1}HNMR at pH 11 in D_2O adjusted by NaOD (Figure 1b).

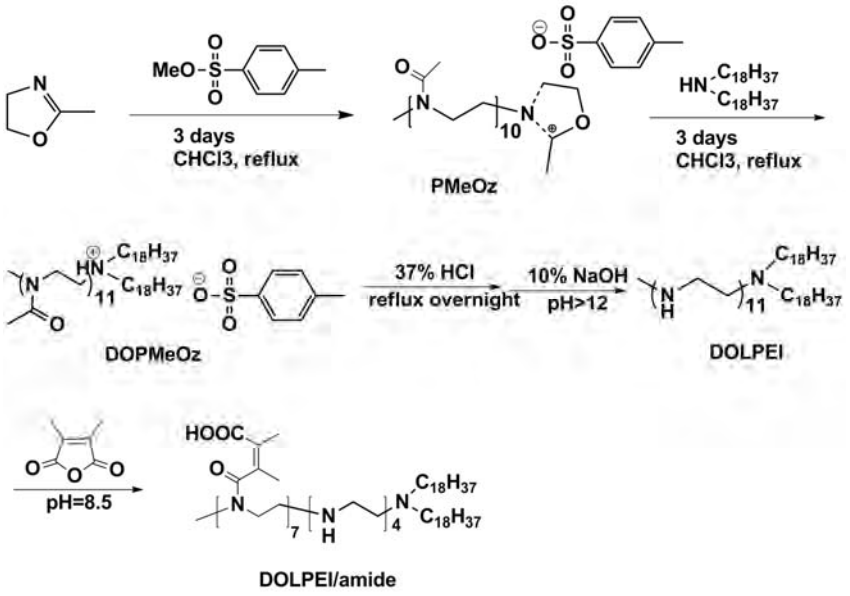

Scheme 2. Synthesis of the cationic lipid dioctadecyl linear polyethyleneimine (DOLPEI) and the subsequent amidization to prepare negative lipid (DOLPEI/amide).

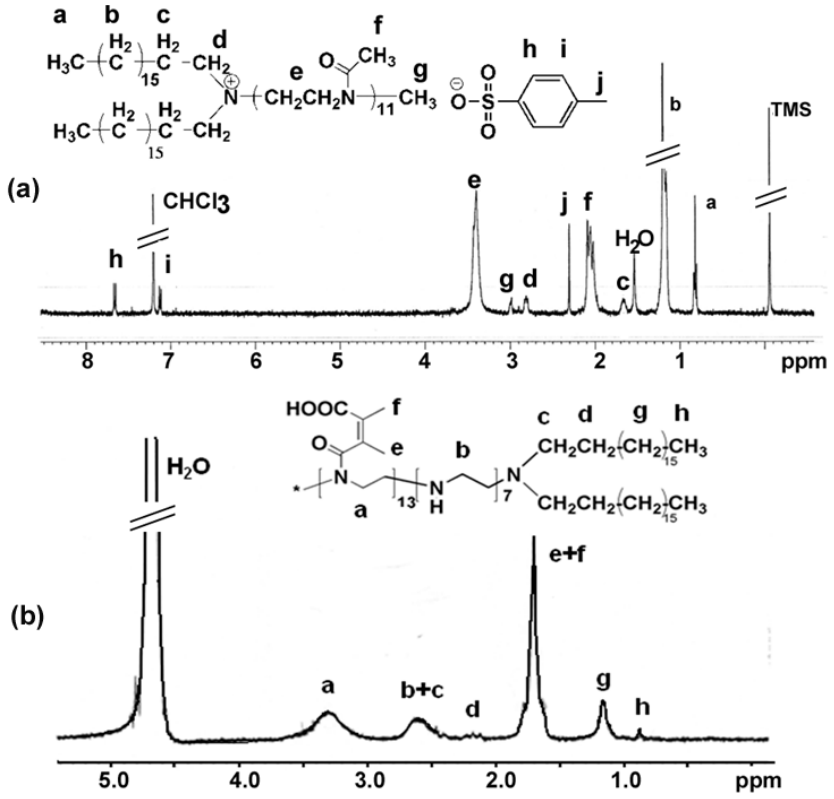

Figure 1. The ^{1}HNMR spectrum of DOPMeOz in $CDCl_3$ and DOLPEI/amide in D_2O at pH 11.

1.1.2 The liposome formation and its DOX·HCl loading

We determined the CMC of DOLPEI/amide liposome was about 40 mg/l by fluorescent method using Nile red as a fluorescent probe at the ex/em wavelengths of 485/525 nm. We continued to load DOX · HCl in the

CRL by a dialysis method and determined the drug loading efficiency was 86.0% and the drug loading content was 17.7%. After that, the pH-dependent drug-release kinetics from the DOLPEI/amide-DOX · HCl liposome (CRL/DOX · HCl) was tested at pH 6 and 7.4 using a dialysis method. As shown in Figure 2, at pH 7.4, only 51.9% of the loaded DOX · HCl was released from the liposome within 12 hours while at pH 6.0, 83.3% of that was released within 6 hours.

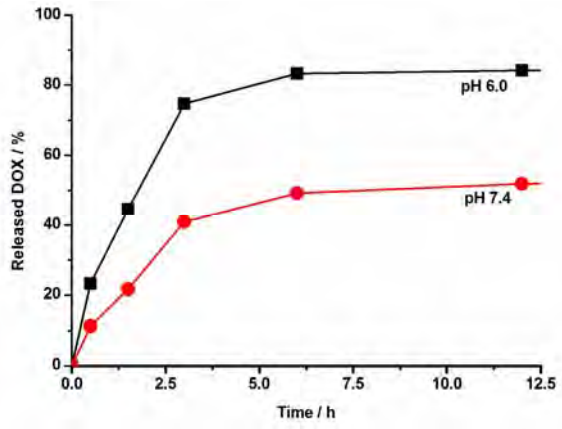

Figure 2. The DOX·HCl release kinetics from the CRL/DOX·HCl liposomes at pH 7.4 and 6.0 at 37 .

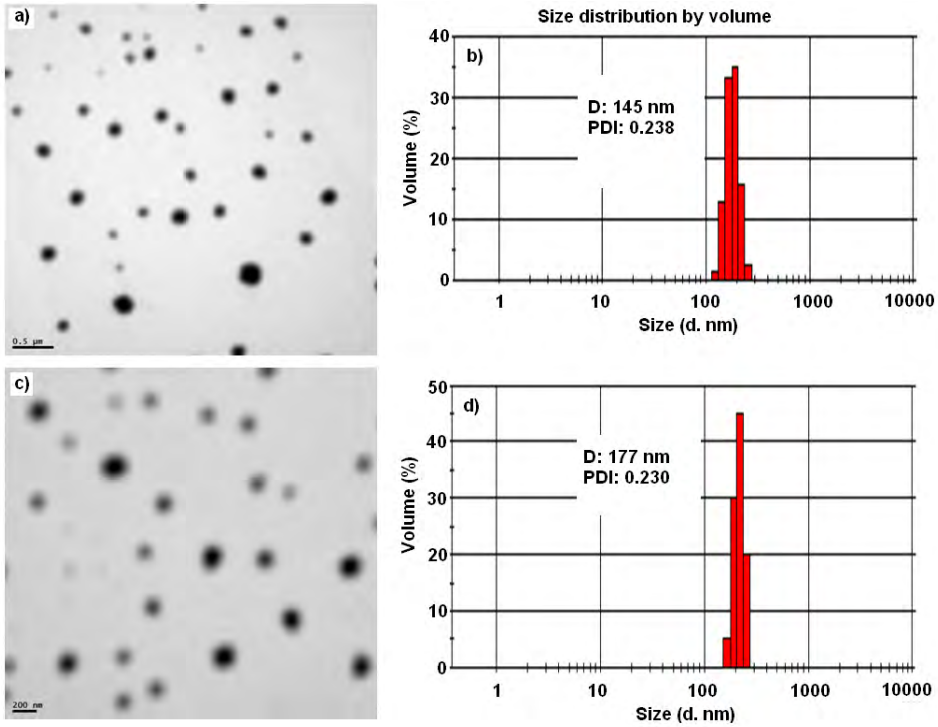

Figure 3. CRL observed by transmission electron microscopy (TEM) (a, scale bar of 500 nm, dyed with phosphotungstic acid stain), and measured by dynamic laser light scattering (DLS) (b). CRL/DOX·HCl observed by TEM (c, scale bar of 200 nm) and measured by DLS (d) (17.7 wt% DOX·HCl).

As shown in Figure 3, the sizes of CRL and CRL/DOX · HCl were measured by nanosizer and confirmed by TEM. The average diameters of the CRL and the CRL/DOX · HCl were 146 and 177 nm, respectively. The TEM images showed the spherical structure of liposome of CRL and CRL/DOX · HCl.

1.1.3 The pH-triggered hydrolysis and charge reversal

The charge reversal of CRL was determined by measuring its ζ- potentials at different acidities. As shown in Figure 4, at pH 7.4, the ζ-potential of CRL was around -15 mV within the first 12 h and still less than -5 mV even after 24 h, indicating that the liposome was always negatively charged as a result of the presence of COOH groups. At pH 5, the ζ-potential of the liposome immediately became highly positive and reached +10 mV within 0.5 h. At pH 6, the ζ-potential of the liposome changed from negative (-15 mV) to positive in 6 h and reached a plateau at about +5 mV in 24 h. Therefore, the liposome was proved as a charge-reversal liposome.

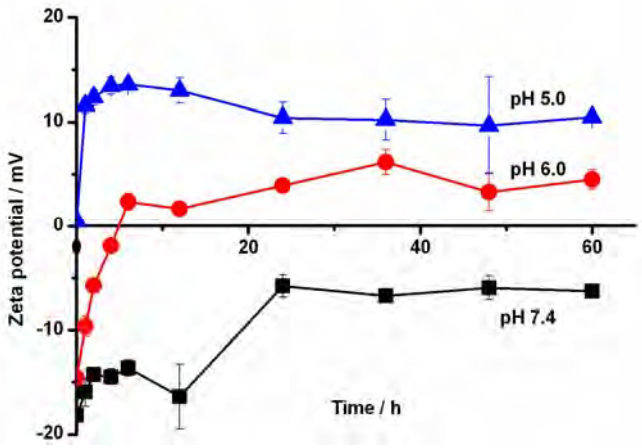

Figure 4. The ξ potential of the CRL at 37 °C as a function of time at different pH values.

1.1.4 Hemolysis

The lysosome-lyzing ability of CRL was estimated using a hemolytic assay of red blood cells (RBCs)[12]. RBCs were incubated with CRL at desired concentrations ranging from 20 to 1000 μg mL^{-1} at 37℃ in different PBS buffers (Table 1). CRL showed almost no hemolytic ability at 400 μg mL^{-1} at pH 7.4 in 12 h. However, after being hydrolyzed for 12 h, the CRL caused 12.18% hemolysis at 400 μg mL^{-1} at pH 6.0 and 10.39% of that at 100 μg mL^{-1} at pH 5. The results demonstrated that CRL had good lysosomal lyzing ability after it retrieved the positive charges in acidic lysosomes (pH 4–5). Therefore, the CRL could escape from the lysosomes.

Table 1. Hemolysis (mean_SD) of sheep RBCs after incubation with different concentrations of the CRL at 37℃ for 12 h (n = 3).

Concentration ($\mu g\ mL^{-1}$)	pH 7.4	pH 6.0	pH 5.0
20	1.48 ± 2.32	0.38 ± 1.69	1.67 ± 2.82
50	0.75 ± 1.87	1.22 ± 1.62	3.71 ± 1.80
100	1.35 ± 1.36	5.29 ± 2.72	10.39 ± 2.18
400	2.42 ± 1.65	12.18 ± 2.03	11.27 ± 1.24
1000	39.66 ± 0.45	53.09 ± 1.44	81.30 ± 3.51

1.1.5 Cellular uptake and subcellular distribution

The cellular uptakes of the CRL/DOX•HCl were quantitatively investigated using flow cytometry. As shown in Figure 5, after pretreated at pH 7.4, the DOX fluorescence intensity of CRL/DOX•HCl was comparable to free DOX•HCl, suggesting the DOX•HCl loaded liposome could enter SKOV-3 cells as efficiently as free DOX•HCl. After it was pretreated for 6 h at pH 5 or 6, the DOX fluorescence intensity significantly increased. These results further confirmed that, once in the acidic extracellular fluid of solid tumor tissues, the CRL carrier would be able to become positively charged and thus attach to the cell membranes, and then be quickly taken up.

A subcellular compartment labeling method was used to observe the subcellular distribution of CRL/DOX・HCl using confocal microscopy (Figure 6). DOX・HCl labeled liposome was expressed as red. Lysosomes were labeled with LysoTracker and displayed as green. Drag 5 was used to label nuclei and displayed as blue. After 6 h incubation, CRL/DOX・HCl was quickly taken up and mostly localized in the lysosomes. Some liposomes not associated with lysosomes probably were those that had already escaped from the lysosomes. With the nuclei stained by DRAQ5, many liposomes were found to be associated with or near the nuclear membrane.

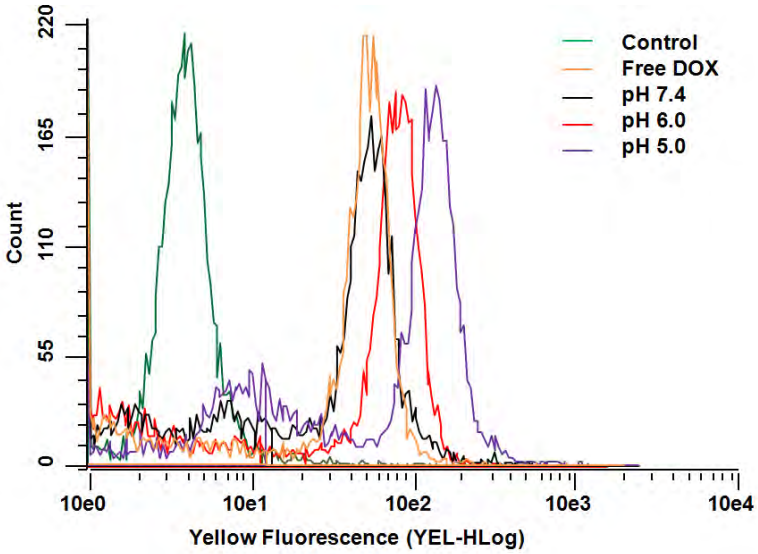

Figure 5. The DOX-positive cell population measured by flow cytometry of SKOV-3 ovarian cancer cells of DOX·HCl (86.3%) and CRL/DOX·HCl prehydrolyzed at pH 7.4 (75.4%), 6.0 (83.7%) and 5.0 (76.9%) for 12 h. Referred from the same control cells (green peak, 0.9%). DOX dose was 1 μg/mL^{-1} and the cell counts were 5000.

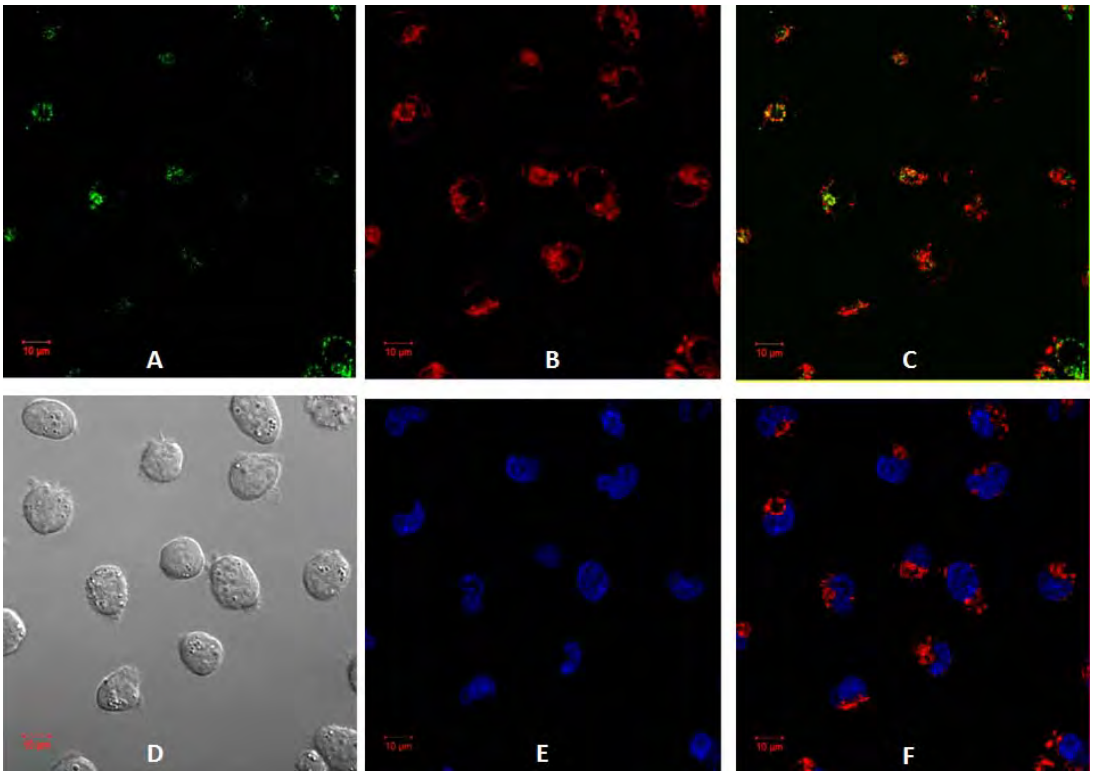

Figure 6. Subcellular localization of CRL/DOX·HCl observed by confocal microscopy. A), LysoTracker green (DND-26, to label lysosomes) channel; B), DOX channel; C) The overlap of A) and B) images; D) Transmittance channel; E) The nuclear dye DRAG5 channel; F): The overlap of B) and E) images. SKOV-3 ovarian cancer cells were incubated for 6 h at 37 ℃ with CRL/DOX·HCl at DOX·HCl equivalent dose of 1 μg mL^{-1}.

1.1.6 In vitro cytotoxicity

The *in vtiro* cytotoxicity of free DOX · HCl, CRL and CRL/DOX · HCl to SKOV-3, MCF-7 and MCF-7/ADR cancer cells was evaluated using the (3-(4,5-dimethylthiazolyl- 2)-2,5-diphenyltetrazolium bromide) (MTT) assay. The cells were treated for 72 h and then post-treated for 24 h to allow the damaged cells undergo apoptosis. As shown in Figure 7, the blank CRL showed no detectable cytotoxicity to the three types of cancer cells even at high doses. The IC_{50} values of the free DOX · HCl were 0.455, 0.161 and 0.464 μg mL^{-1} to SKOV-3, MCF-7 and MCF-7/ADR cells, respectively. However, the CRL/DOX · HCl with the smaller IC_{50} values (0.216 μg mL^{-1} for SKOV-3 cells, 0.035 μg mL^{-1} for MCF-7 cells and 0.221 μg mL^{-1} for MCF-7/ADR cells) exhibited a higher cytotoxicity than free DOX · HCl . This is much advanced to the majority of DOX loaded liposomes previously reported[13, 14].

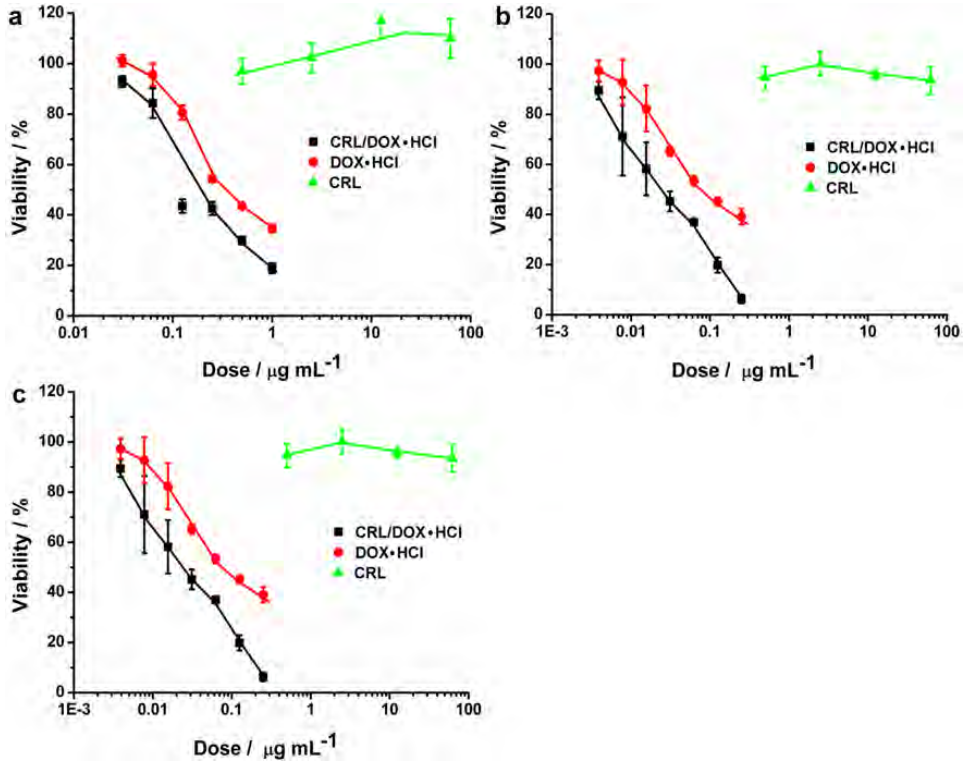

Figure 7. The cytotoxicity of DOX·HCl, CRL/DOX·HCl and CRL to SKOV-3 ovarian cancer cells (a), MCF-7 (b) and MCF-7/ADR (c) breast cancer cells as a function of the DOX·HCl or CRL dose. Cells were exposed to the indicated drug or liposome for 72 h. Data represent mean ± s.d., n=5.

1.1.7 Conclusion

We demonstrated a negative-to-positive charge-reversal liposome for cancer drug targeted delivery. The liposome was negatively charged at physiological pH and gradually becomes positively charged at pH 6 and

quickly highly positively charged at pH 5. Such charge reversal can effectively enhance the cellular uptake of the liposomes and exhibit higher cytotoxicity to cancer cells, showing a great promise for *in vivo* administrations.

1.2 Nuclear drug delivery by a charge-reversal TAT peptide

Cell-penetrating peptides (CPPs) such as transactivator of transcription (TAT) peptide have long been explored for promoting *in vitro* cell penetration[15, 16] and nuclear targeting of various cargos[17, 18], but their positive charges cause strong nonspecific interactions[19, 20], making them inapplicable for many *in vivo* applications. Although there are several approaches have been proposed to shield the cationic charges of CPPs, including fusing with an anionic peptide[21], complexing with an acid-sensitive polymer[22] or DNA[23], and using a "pop-up" method burying TAT in the hydrophilic PEG corona at neutral pH but exposing at acidic pH[24], they all have limitations in real *in vivo* administrations.

Herein, we used a molecular modification strategy for CPPs *in vivo* applications[25]. We demonstrated that the amidizing of the lysine residue amines to acid-labile amides would inactive the CPPs in bloodstream and the hydrolyzing of the acid-labile amides in tumor interstitium (pH<7) or cell endo/lysosomes (pH = 4-5) would activate the CPPs and expose their functions (Figure 8a). We tethered an arginine-rich TAT peptide and its amidized product, denoted as ^{a}TAT, to the corona of PEG-PCL micelles (Figure 8b) and compared the in vitro and in vivo properties of the resulting functionalized micelles (TAT-PEG-PCL and ^{a}TAT-PEG-PCL).

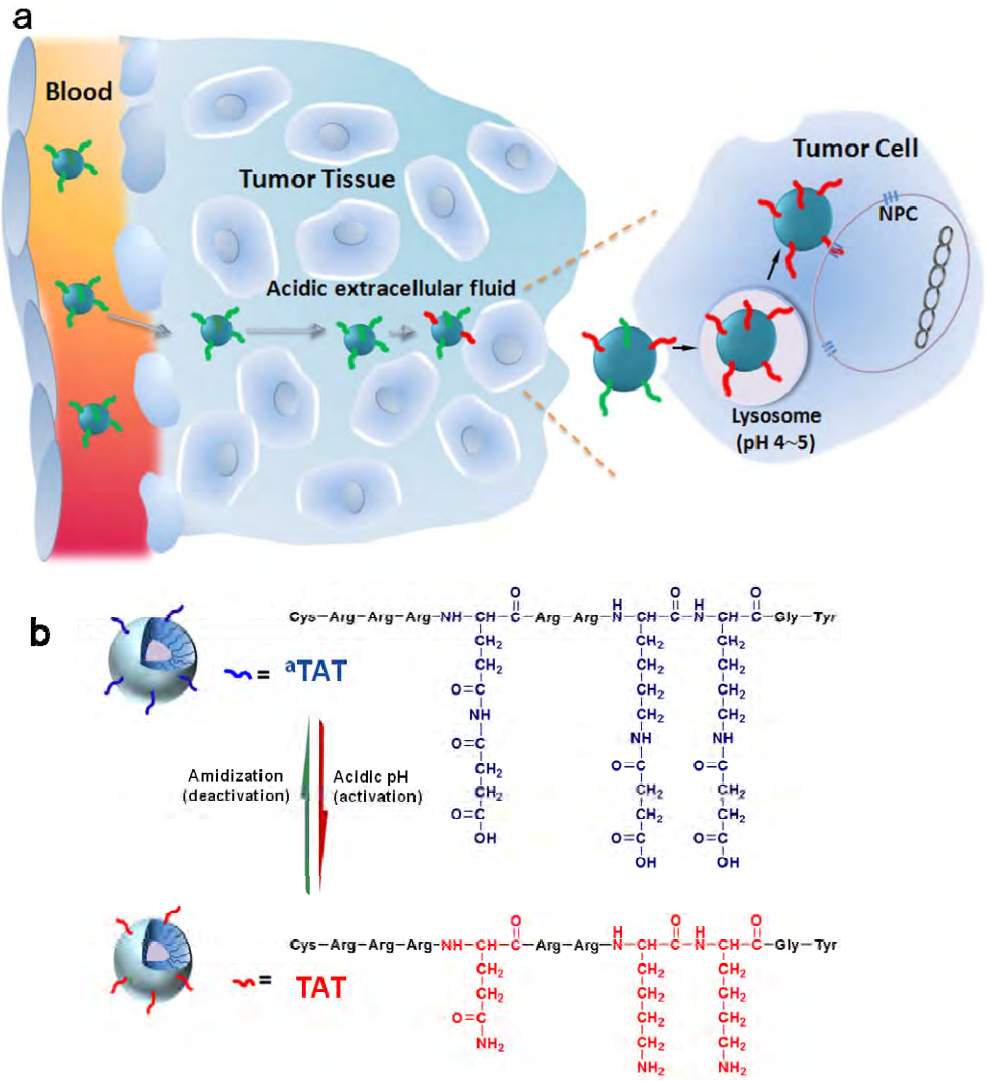

Figure 8. (a) Illustration of the use of TAT as an example of a cell-penetratingpeptide (CPP) to demonstrate the concept of deactivation of a CPP in the blood compartment and its activation in the tumor interstitium or cells for *in vivo* tumor-targeted drugdelivery. (b) Amidization of TAT's primary amines to succinyl amides and their acid-triggered hydrolysis.

1.2.1 TAT amidization and micelle functionalization

We amidized the TAT lysine residue amines using an excess of succinyl chloride and characterized the produced ^{a}TAT by MALDI-TOF mass spectrometry. The stability of ^{a}TAT was evaluated by monitoring its hydrolysis at pH 5.0 using HPLC. After the TAT- or ^{a}TAT-functionalized PEG-PCL copolymers were synthesized, micelles functionalized with TAT or ^{a}TAT were fabricated and optimized by dialysis of a mixture of PEG-PCL with TAT-PEG-PCL or ^{a}TAT-PEG-PCL at the ^{a}TAT-PEG-PCL/PEG-PCL molar ratio of 15/85, resulting in the size around 70 nm in diameter.

1.2.2 Cellular internalization and intracellular distribution

As shown in Figure 9, the PEG-PCL/DOX micelles entered SKOV-3 cells very slowly while the TAT-PEG-PCL/DOX micelles entered cells very quickly. The cellular uptake of ^{a}TAT-PEG-PCL/DOX micelles was very similar to that of PEG-PCL/DOX and significantly slower than that of TAT-PEG-PCL/DOX, indicating the ^{a}TAT could not interact with the cells as pristine TAT did. However, once ^{a}TAT-PEG-PCL micelles were first incubated at pH 5.0 for 8 h, their cellular uptake became as fast as that of TAT-PEG-PCL/DOX, suggesting the recovery of fully functioning TAT moieties on the micelle surface.

We used live cells for fluorescence microscopy studies observing the cellular uptake and subsequent intracellular distribution (Figure 10). Nile red, instead of DOX, was used to trace the micelles. In agreement with the flow cytometry results, the cellular uptake of TAT-PEG-PCL/nile red was much faster than that of PEG-PCL/nile red. The cellular internalization of ^{a}TAT-PEG-PCL/nile red was also very similar to that of PEG-PCL/nile red at short incubation times; however, more and more red dots were found in the cells when the culture time was prolonged to 12 or 24 h. The internalized micelles were found initially to be localized in the lysosomes, where ^{a}TAT could hydrolyze and regenerate TAT. After incubation for 5 h, many micelles were no longer located in the endo/lysosomes, suggesting successful escape from the endo/lysosomes. Furthermore, many ^{a}TAT-PEG-PCL micelles were found punctuated on the nuclear membranes, particularly after 24 h. Thus, such results confirmed that once internalized into a lysosome, the ^{a}TAT on the micelle was regenerated into TAT, which enabled the micelle escape into the cytosol, traverse to the perinuclear region, and subsequently bind the nuclear pore complexes.

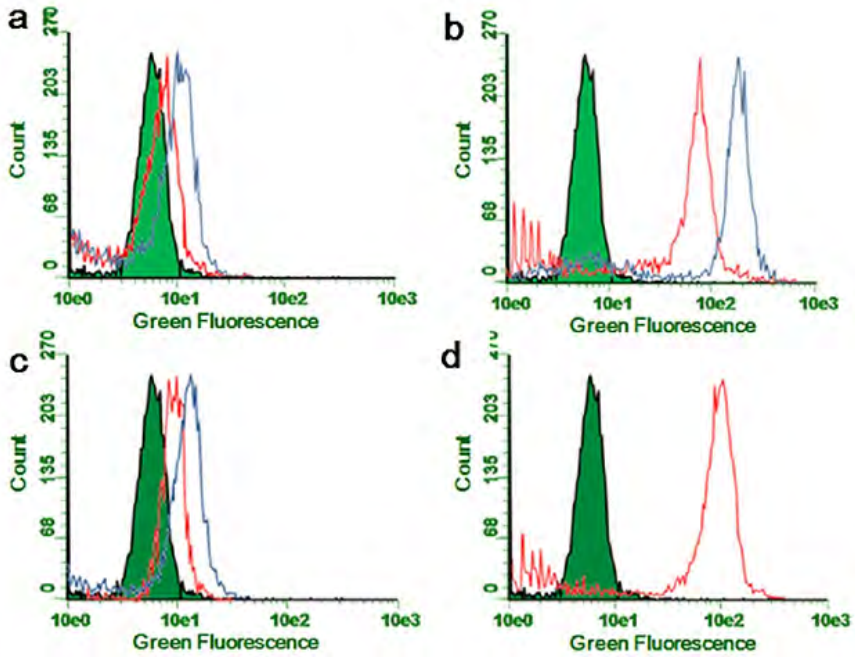

Figure 9. DOX-positive cell populations measured by flow cytometry of SKOV-3 ovarian cancer cells cultured with (a) PEG-PCL/DOX for 1 h (red curve, 3.2%) and 5 h (blue, 15.3%), (b) TAT-PEG-PCL/DOX for 1 h (red curve, 58.6%) and 5 h (blue, 73.7%), (c) [a]TAT-PEG-PCL/DOX for 1 h (red curve,7.8%) and 5 h (blue, 21.2%), and (d) [a]TAT-PEG-PCL/DOX (preincubated at pH 5.0 for 8 h) for 5 h (red curve, 64.2%). All of the populations are referenced to the same control cells (green-shaded peaks, 0.8%). The DOX dose was 1 μg/ml.

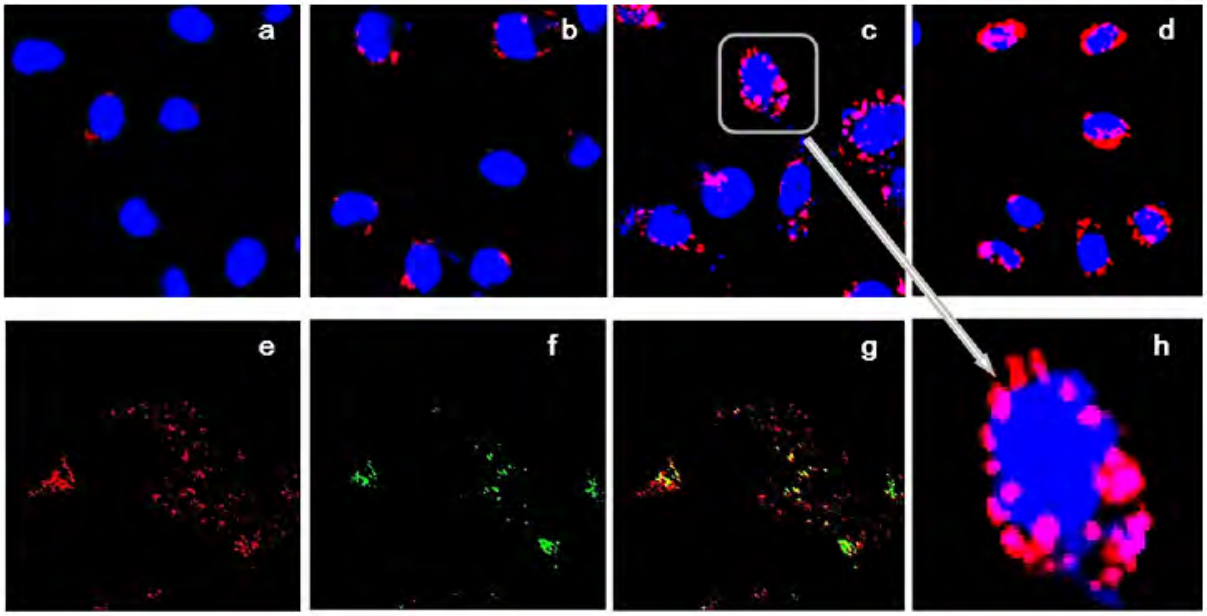

Figure 10. Cellular uptake and intracellular localization of [a]TAT-PEG-PCL/nile red micelles observed by confocal microscopy. SKOV-3 ovarian cancer cells were cultured with [a]TAT-PEG-PCL/nile red at a nile red dose of 1 μg/ml for (a) 1, (b) 5, (c) 12, and (d) 24h. An amplification of one cell in (c) is shown in (h). Lysosomal colocalization of [a]TAT-PEG-PCL/nile red in the cells after incubation for 5 h at 37 °C was observed by confocal microscopy through (e) the nile red channel and (f) the LysoTracker green channel. The overlap of the images in (e) and (f) is shown in (g). The nuclei were stained with DRAQ5 (blue). Nile red-loaded micelles appear in red and lysosomes stained with LysoTracker in green.

1.2.3 In vitro cytotoxicity

As shown in Figure 11, DOX delivered by ^{a}TAT-PEG-PCL and PEG-PCL micelles exhibited very similar cytotoxicities toward non-drug-resistant Bcap-37 breast cancer cells that were much lower than the cytotoxicity of free DOX. However, free DOX at doses less than 8 μg/ml showed little cytotoxicity toward DOX-resistant MCF-7 cells while DOX loaded in ^{a}TAT-PEG-PCL micelles showed dose-dependent cytotoxicity with an IC_{50} of 2 μg/ml, slightly better than that of PEG-PCL/DOX. To enhance the cellular uptake and elucidate the regeneration of TAT in endo/lysosomes, folic acid (FA) was introduced into the micelles as a targeting group. The cytotoxicities of DOX delivered by ^{a}TAT-PEG-PCL and (FA/^{a}TAT)-PEG-PCL were compared using SKOV-3 ovarian cancer cells over expressing folate eceptors induced by culturing them with folate-free medium. As shown in Figure 11c, (FA/^{a}TAT)-PEG-PCL/DOX had much higher cytotoxicity than ^{a}TAT-PEG-PCL/DOX and even free DOX, even though this cell line is not DOX-resistant.

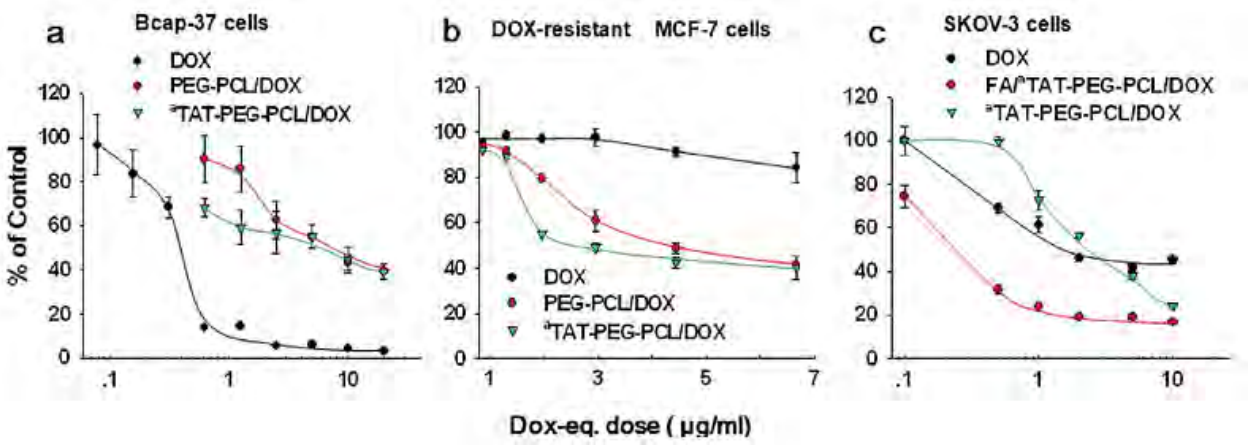

Figure 11. Cytotoxicities of DOX and DOX-loaded micelles toward (a) non-drug-resistant Bcap-37 breast cancer cells, (b) DOX-resistant MCF-7 breast cancer cells, and (c) folate-receptor-overexpressing SKOV-3 ovarian cancer cells. The cells were treated with DOX or DOX-loaded micelles for 24 h followed by 24 h postculture before analysis by MTT assay [n = 3, data expressed as average ± standard error (SE)]. SKOV-3 cells were cultured in folate-free medium for at least 2weeks before the experiment.

1.2.4 In vivo stability and tumor-targeted drug delivery of amidized TAT

The *in vivo* stability of ^{a}TAT was evaluated by monitoring the blood clearance of the corresponding micelles (Figure 12a). A near-IR fluorescence dye, DiR, was loaded in the micelles as a tracer since the excitation and emission wavelengths of DiR do not overlap with the autofluorescence of blood. The i.v.-injected TAT-PEG-PCL micelles were rapidly cleared from the blood stream. In contrast, ^{a}TAT-PEG-PCL/DiR had a

very slow clearance profile similar to that of PEG-PCL/DiR. These results indicated that [a]TAT indeed caused no nonspecific interactions with the blood component and that the succinyl amides in [a]TAT are very stable in blood.

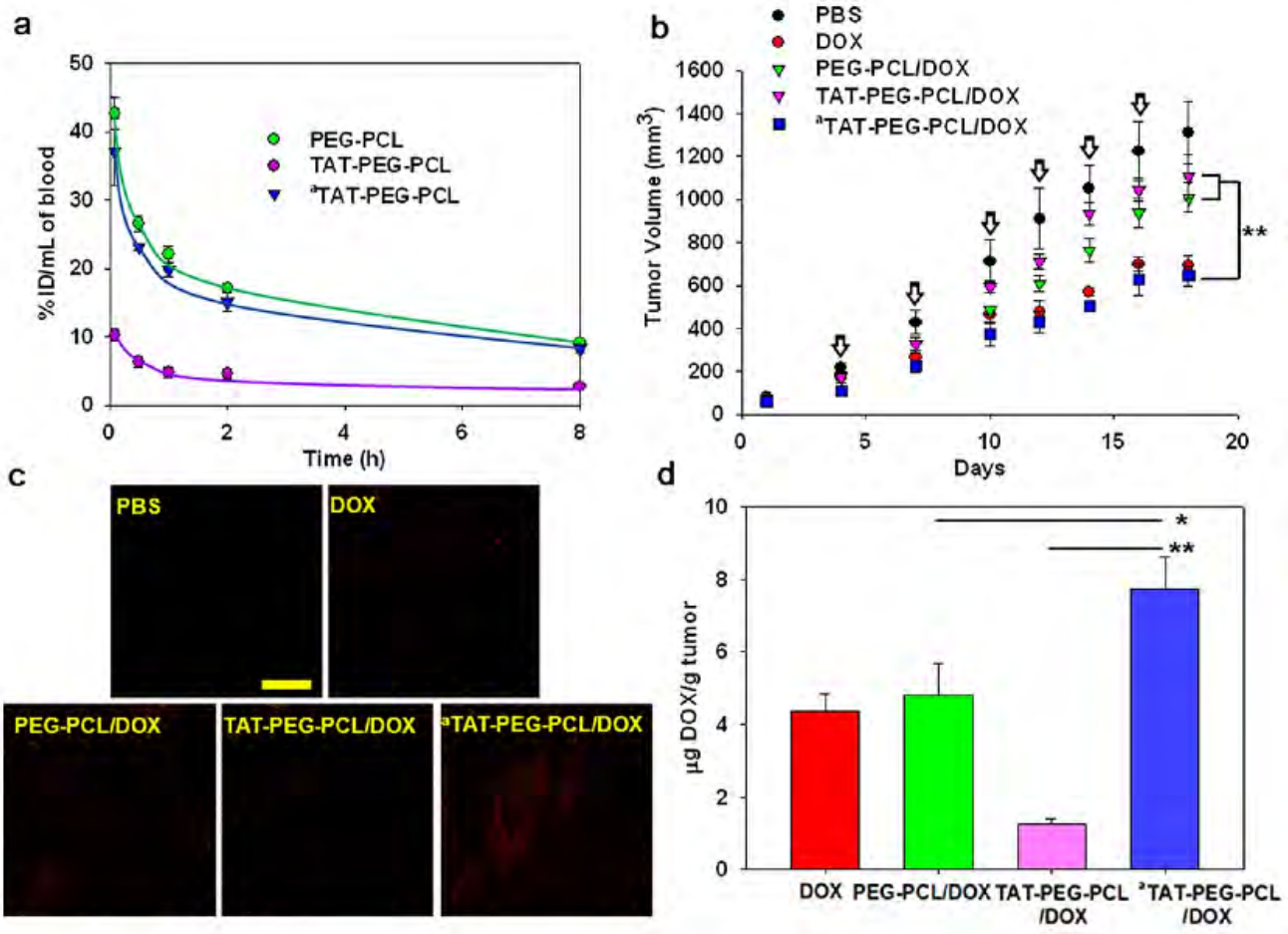

Figure 12. (a) Blood clearance of the micelles, (b) *in vivo* tumor inhibition of DOX and DOX-loaded micelles, and (c,d) their DOX accumulations in tumors (c) as observed by confocal microscopy or (d) as quantitated in terms of micrograms of DOX per gram of tumor tissue.

The accumulation in tumor tissues and therapeutic efficacy of DOX delivered by the micelles were subsequently tested using a xenograft tumor model (Figure 12b). The tumor growth of mice administrated with [a]TAT-PEG-PCL/DOX was much slower than that of mice treated with TAT-PEG-PCL/DOX or PEG-PCL/DOX, and this difference became more significant ($p < 0.01$) after day 15. After the mice were sacrificed, the tumors were dissected and weighed. Thus, compared with TAT-PEG-PCL/DOX and PEG/PCL/DOX, [a]TAT-PEG-PCL/DOX showed a significantly ($p < 0.05$) enhanced therapeutic efficacy. Further observation of the tumor sections by confocal microscopy (Figure 12c) showed that there was more DOX in the tumors treated with [a]TAT-PEG-PCL/DOX than in the other tumors. Quantitation of DOX in the homogenized dissected tumors

showed that [a]TAT-PEG-PCL/DOX-treated tumors had twice the DOX concentration of tumors treated with PEG-PCL/DOX or DOX and about 8-fold that of tumors treated with TAT-PEG-PCL/DOX (Figure 12d).

1.2.5 Conclusion

Using TAT as an example, we have demonstrated herein an efficient molecular modification approach that involves reversible blocking/activation of cationic CPPs. Amidization of the CPPs' lysine residues to succinyl amides can efficiently block their *in vivo* nonspecific interactions; once the amides are hydrolyzed in an acidic environment such as tumor extracellular fluids or endo/lysosomes, theCPPs' membrane-transduction and nuclear-localization activity are fully recovered. Compared with cationic charge-shielding approaches, the amidized CPPs are very stable and have completely inhibited nonspecific interactions in the blood compartment. Thus, coupled with tissue-specific targeting groups, this approach may greatly widen the door for *in vivo* applications of CPPs.

2. Synthesis of degradable dendrimers and its applications for drug delivery

2.1 Synthesis of degradable polyester dendrimers for drug delivery

Dendrimers are highly branched macromolecules characterized by monodispersity, uniform and controlled sizes and copious surface functionalities[26, 27], which make them ideal nanocarriers for biomedical applications[28]. However, conventional used PAMAM dendrimers are not degradable and carry positive charges on their surface, thus inducing cytotoxicity[29, 30], hemolytic toxicity[31], rapid blood clearance[31] and quick opsonization (RES)[32]. These drawbacks hinder their translation to clinical applications. Aliphatic polyester dendrimers, for example, the dendrimers from an AB_2-type monomer 2,2-bis(hydroxymethyl)propionic acid (bis-MPA), are biodegradable and biocompatible with very low toxicity and low immunogenicity[33, 34], and thus have been proposed as carriers for biodelivery or *in vivo* imaging[35-39]. However, the syntheses of traditional polyester dendrimers consist of protection/deprotection[40] is tedious and incomplete and thus introduce defects amplified in the subsequent generations[41-45].

Taking advantage of highly efficient thiol/acrylate Michael addition reactions, we developed a simple but efficient strategy to synthesize bis-MPA-based dendrimers without any protection/deprotection steps[46]. The

monomers were easily obtained and the reactions were fast under mild conditions. A dendrimer with 128 terminal hydroxyl groups was constructed in five steps (Scheme 3) with a high overall yield.

2.1.1 Synthesis of degradable polyester dendrimers

The hydroxyl groups in bis-MPA must be protected first to avoid self-esterification or convert to other functional groups that cannot cause cross-linking[42, 47]. A monomer pair of thioglycerol (AB2) and ACPA (CD2) simplified the reaction requiring no protection/deprotection steps. The Michael addition reaction of thiol−acrylate is almost quantitative without side reactions and considered to be a click reaction in polymer synthesis[48-50] and functionalization[51, 52]. Different from the radical mechanism of the thiol−ene/yne reactions, the thiol−(meth)acrylate reaction does not involve radicals, avoiding side reactions via radical coupling.

The PTA was first reacted with the thiol group in thioglycerol to produce the first-generation dendrimer with eight hydroxyl groups (Scheme 3, step i). Pendant hydroxyl groups were esterified with ACPA with catalysis of DIC/DMAP (Scheme 3, step ii). Alternating the two steps easily produced the fifth generation of the dendrimers at high overall yields (68%).

The reaction between PTA and a slight excess of 1-thioglycerol in the presence of a catalytic amount of the triethylamine was carried out at room temperature. Completion of the acrylate groups' reaction was confirmed by ^{1}HNMR and MALDI-TOF mass spectra. Simple precipitation of the solution in ethyl ether removed the unreacted 1-thioglycerol, yielding the pure first generation (G1-$_{8OH}$). G1-$_{8OH}$ was then reacted with ACPA catalyzed by the DIC/DMAP coupling agents. The esterification of G1 was monitored using MALDI-TOF analysis to ensure completion. We found that a three-to-one ratio of ACPA relative to each hydroxyl group (COOH/OH = 3) was needed to complete the esterification and produce the target G2-$_{16acrylate}$. DIC and G2-$_{16acrylate}$ are soluble in ether, but the product of N,N'-diisopropylurea is not. Therefore, G2-$_{16acrylate}$ was easily isolated by ether extraction and precipitation.

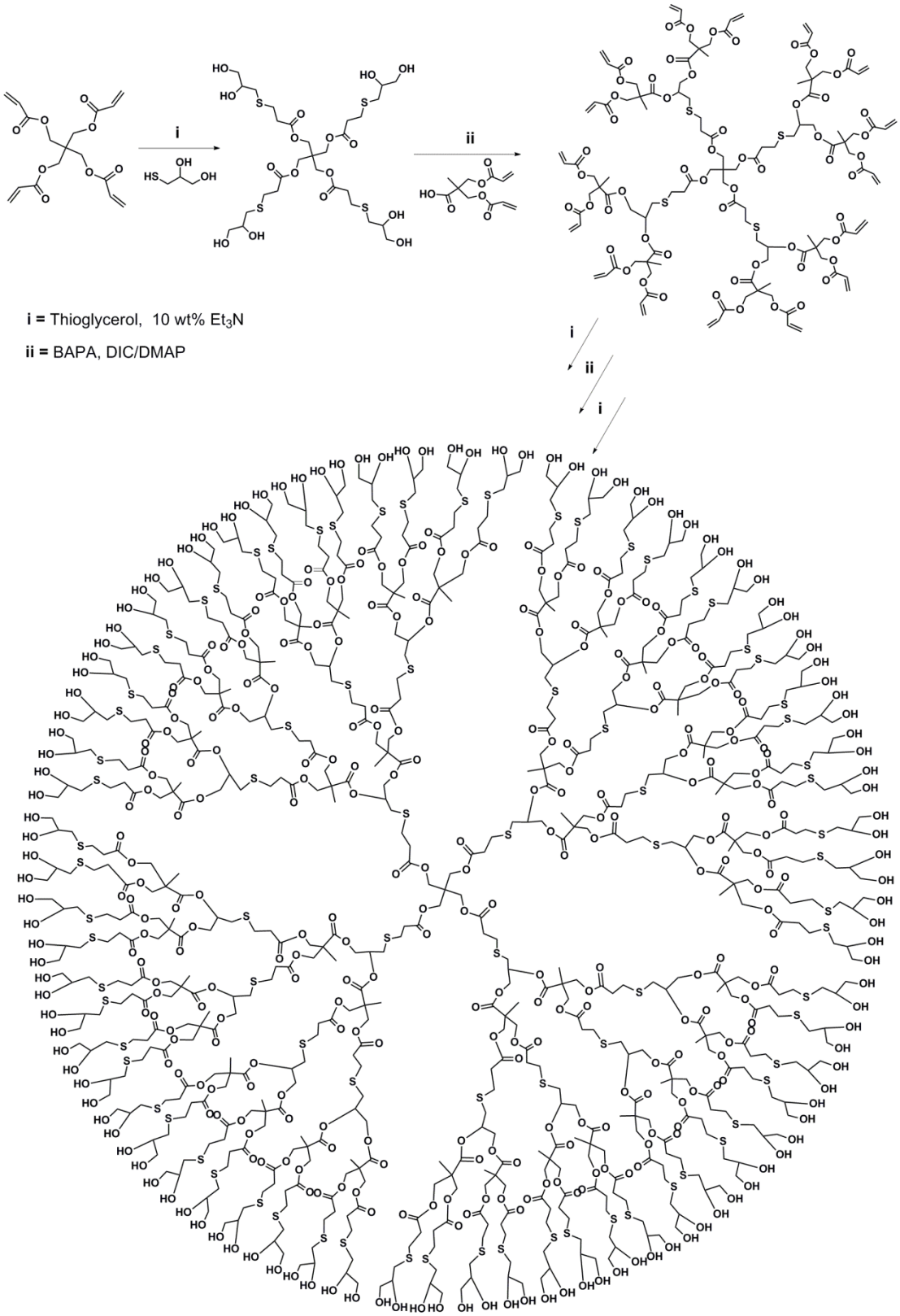

Scheme 3. Dendrimer Synthesis from a AB_2 Monomer Pair 2,2-Bis(acryloyloxymethyl)propionic Acid (ACPA) and 1-Thioglycerol.

2.1.2 Characterizations of degradable polyester dendrimers

Figure 13 shows the MALDI-TOF MS spectra of the reaction solutions. Clearly, the reaction solution in

each generation only contained the targeted dendrimer molecules in agreement with the calculated molecular weight. There were almost no signals of incomplete molecules. The MALDI-TOF spectrum of the fifth generation had a poor resolution due to difficult evaporation as a result of its high molecular weight. However, its GPC trace was as narrow as that of the prior generation, and DLS showed that it had a diameter of 5.2 nm in water with a low PDI, indicating the fifth generation also had similar perfect structure. The typical ^{1}HNMR spectra of the acrylate- and hydroxyl-terminated dendrimers (G4-$_{64acrylate}$ in $CDCl_3$ and G5-$_{128OH}$ in DMSO-d_6) are shown in Figure 14.

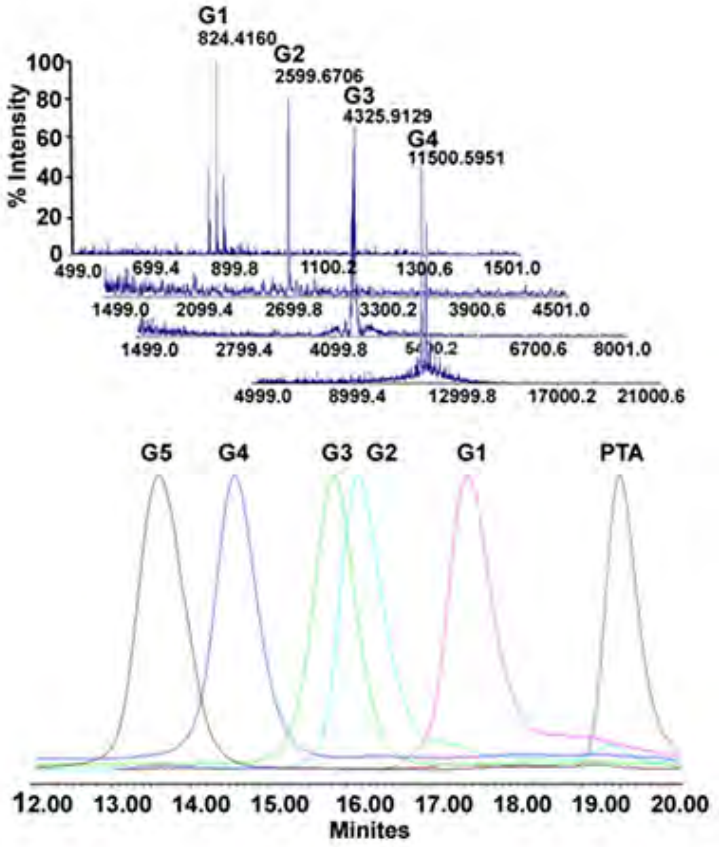

Figure 13. Molecular-weight progress of the dendrimers from the reaction of ACPA and thioglycerol measured by (a) MALDI-TOFMS and (b) GPC. The MALDI-TOFMS spectra were obtained from the reaction solutions without any purification.

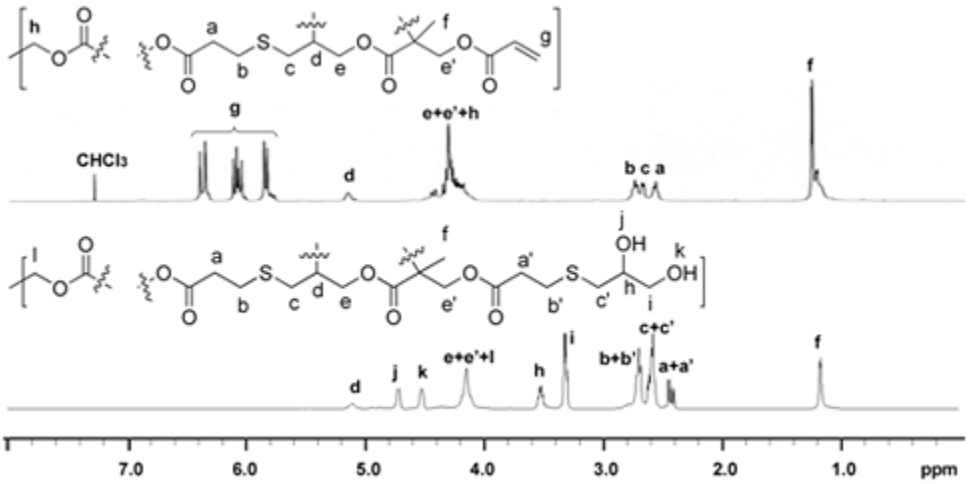

Figure 14. [1]HNMR spectra of G4-$_{64acrylate}$ (in $CDCl_3$) and G5-$_{128OH}$ (in DMSO-d_6).

The hydroxyl-terminated dendrimers were water-soluble at room temperature. G1-$_{8OH}$ andG3-$_{32OH}$ remained water-soluble at a high concentration (up to 5 wt%) at high temperatures (up to 80 °C) (Figure 15). Upon increasing the temperature higher than 41 °C, the clear solution of G5-$_{128OH}$ dendrimer suddenly became cloudy and the dendrimer precipitated. This soluble/insoluble transition at the lower critical solution temperature (LCST) was generally due to the disturbance of hydrophilicity/hydrophobicity balance of the polymer chains[53, 54]. This phenomenon was consistent with our recent results of thermally responsive polyester dendrimers[54].

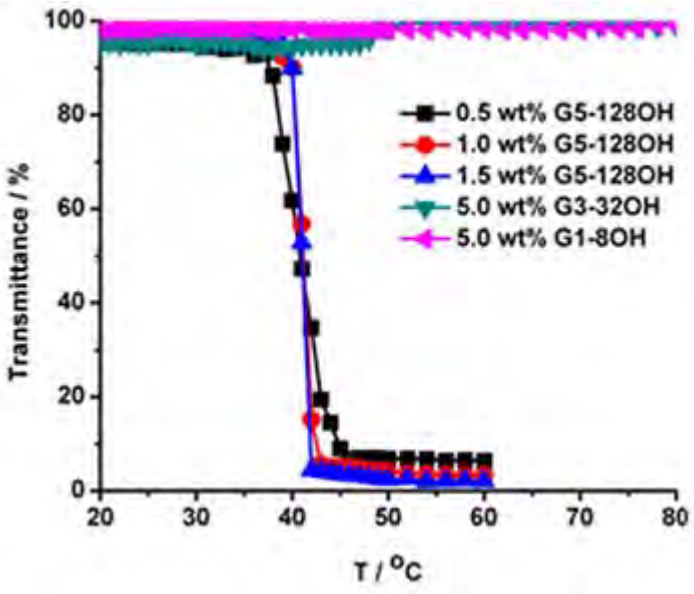

Figure 15. Transmittance of the solutions of G1-$_{8OH}$, G3-$_{32OH}$, and G5-$_{128OH}$ in DI water as a function of temperature at different concentrations.

We introduced PEG 2kDa chains on to the dendrimer surface of G5-$_{128OH}$ to further grant it stealth properties as a drug carrier. The biocompatible dendrimer G5-$_{PEG}$ showed an excellent capacity for the

encapsulation and controlled release of a hydrophobic anticancer drug such as DOX.

2.1.3 Conclusion

We successfully developed an efficient synthesis of monodispersed bis-MPA polyester dendrimers using thiol−acrylate reaction and the traditional esterification reaction under mild conditions. The simple synthesis and purification make the dendrimer synthesis straight forward for large-scale production. Furthermore, the hydroxyl-terminated dendrimers were thermoresponsive, and the LCST was 41 °C, which is near the physiological temperature. The modified G5-PEG showed a promise as a drug carrier for cancer chemotherapy.

2.2 Synthesis of degradable bifunctional dendritic polymers for drug delivery

Dendrimers are synthesized by multistep reactions of multifunctional monomers[55, 56]. Generally, all the functional groups are used to construct the dendrimers, and thus there are no reactive groups left in the interior. Therefore, most dendrimers have nonreactive interiors, serving simply as the skeleton of the nanostructure, and reactive peripheries with functional groups such as amine, carboxylic acid, hydroxyl, or unsaturated double bonds available for functionalization[57, 58]. Thus, drugs, peptides, targeting groups, or polymer chains are generally introduced on the peripheries to obtain dendrimer–drug conjugates[59, 60]. In these dendrimer conjugates, drug moieties tethered to the periphery can contact and thus interact with blood components such as the lipophilic domains of proteins in the blood, causing opsonization. The drug-loading contents of the tethered hydrophobic drugs also cannot be high, generally several percent, to keep the dendrimer conjugates water soluble[61]. When the dendrimer interiors are used to encapsulate drugs, the low drug-loading content and burst release are the two major problems[62].

Interior-and-periphery bifunctional dendrimers can make full use of the nanostructures36. We proposed interior and peripheral bifunctional polyester dendrimers as versatile and biodegradable drug carriers whose interior functional groups might be used for drug conjugation while the periphery might be PEGylated for stealth properties. Herein, we report a convenient synthesis of these bifunctional dendritic polyesters with a high density of functionalities via sequential thiol/acrylate Michael addition reaction from A_3 (triacrylates) and B_2C_2 (dithiothreitol, C=OH) types of monomers[63]. The resulting dendritic polymers had peripheral acrylate groups and interior hydroxyl groups.

2.2.1 Synthesis of degradable bifunctional dendritic polymers

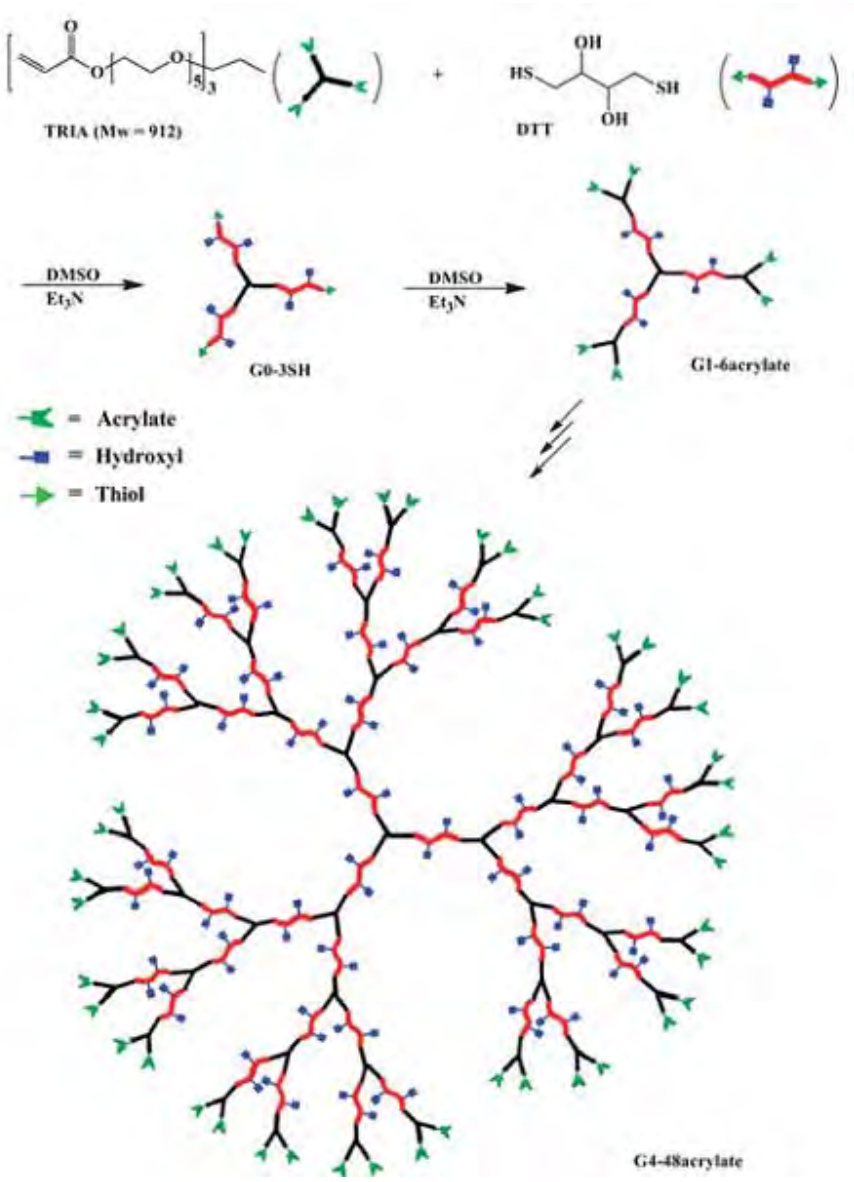

Scheme 4. Synthesis of degradable bifunctional dendritic polymers from TRIA and DTT.

To synthesize dendrimers with interior functionalities, the monomer(s) must contain either protected functional groups or functional groups that do not participate in the dendrimer synthesis reactions. DTT contains two highly reactive thiol groups and two hydroxyl groups. Michael addition reactions of thiols with acrylates and other electron-deficient enes are particularly efficient but simple. Thus, no protection/deprotection is needed when using the DTT–acrylate reaction to prepare interior hydroxy-functionalized dendritic polymers. We chose the readily available A_3-type monomer TRIA[52] (Mn 912) and DTT (B_2C_2 type) as a pair of monomers. As shown in Scheme 4, TRIA was first used as the core-forming compound to react with an excess of DTT (thiol/acrylate = 4) and obtained the thiol-terminated core G_0-3SH. It was then reacted with an excess of

A_3 monomer TRIA (acrylate/SH = 4) to produce the acrylate-terminated first generation (G_1-6acrylate) with 6 hydroxyl groups in the interior. Alternating addition of the two monomers produced the fourth-generation dendritic polymer(G_4-48acrylate) with ninety interior hydroxyl groups at a high overall yield (62%). The GPC traces of the four dendritic polymer generations are shown in Figure 16. Their molecular weight gradually increased as the generation increased from 1 to 4, and were very close to their calculated values.

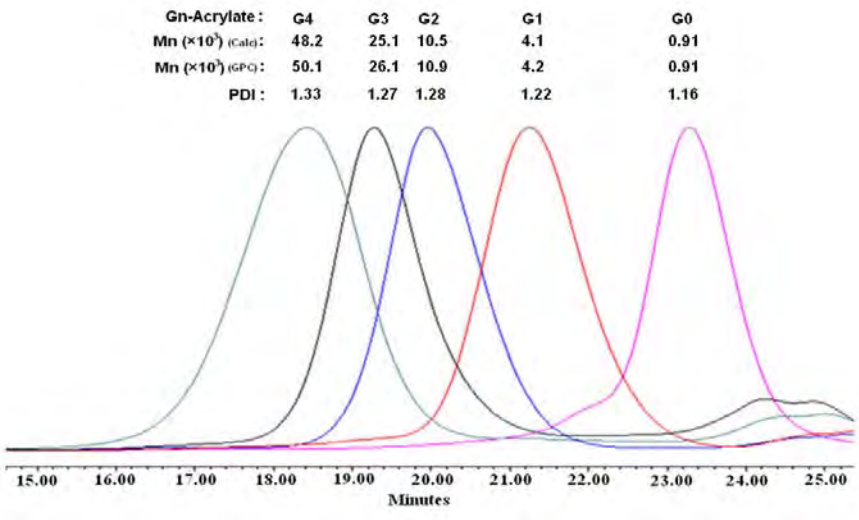

Figure 16. GPC traces of the dendritic polymers from G_0 to G_4.

Due to the equal reactivity of the two thiol groups in DTT and the three acrylate groups in TRIA, an excess of a monomer had to be used to avoid crosslinking to create a low-polydispersity dendritic polymer. The solvent was also found to play an important role in the synthesis. The reaction of thiol/acrylate was too fast in DMSO and thus caused crosslinking even in the presence of much excess of DTT. The reaction was slow in dichloromethane. Thus, a mixed solution of dichloromethane/DMSO at the ratio of 10:1 was found to give an optimal reaction rate. Most reactions could be completed within 6 hours at room temperature. The thiol/acrylate ratio was subsequently optimized. The resulting products were characterized by ^{1}HNMR and GPC. While the dendritic polymers had thiol or acrylate functional groups on their periphery, they also contained hydroxyl groups in their interiors and thus the total number of functional groups increased quickly with generation. More importantly, the two types of functional groups are so different as to allow for selective modifications on the surface and the interior.

2.2.2 Synthesis of G4-CPT-PEG

To demonstrate their drug carrier abilities, the fourth-generation dendritic polymer was PEGylated with PEG2k on the periphery and an anticancer drug camptothecin (CPT) was tethered in its interior (Scheme 5). This interior drug conjugation not only avoids burst drug release, but also hides the drug inside the dendritic polymer, preventing its interaction with serum proteins generally found in drug conjugation on the dendrimer periphery.

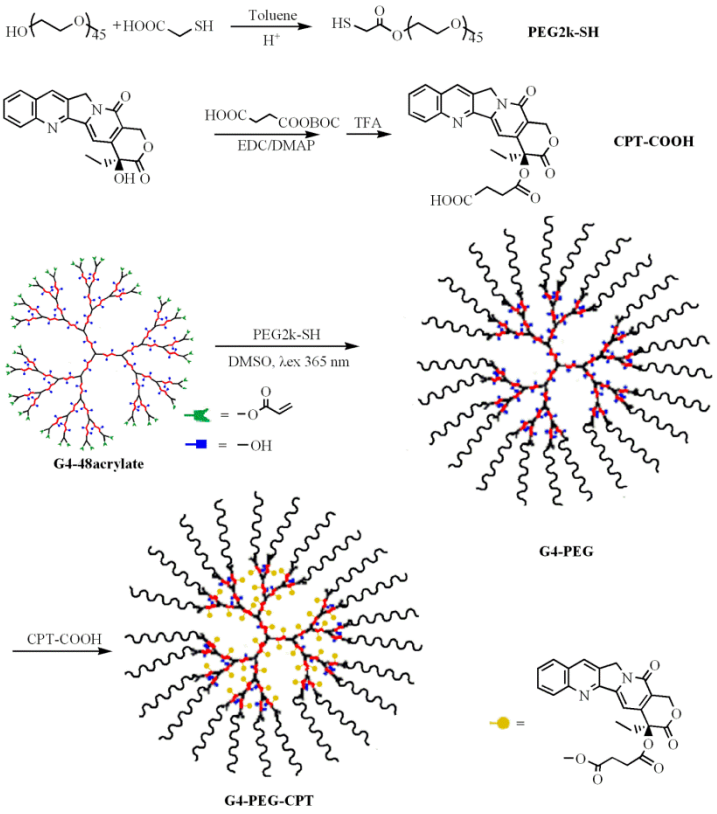

Scheme 5. Surface PEGylation and interior conjugation of CPT of G_4.

PEG2k with a terminal thiol group (PEG2k-SH) was first synthesized by esterification from PEG2k and thioglycolic acid in the presence of a catalytic amount of sulfuric acid. An excess of PEG2k-SH (2 equivalents) was reacted with the G4-48acrylate by UV radiation at 365 nm in the presence of 5 wt% of a photo initiator, DMPA, or direct Michael addition catalyzed by TEA at room temperature. Both approaches could complete the reaction to produce PEGylated G4 (G4-PEG). Hydroxyl groups in the interior of G4-PEG were reacted with CPT–COOH. The conjugation was characterized by ^{1}H-NMR spectroscopy and UV spectra. The CPT content in G4-CPT-PEG was calculated from the integrations of methyl groups in the dendritic backbone and CPT and confirmed by UV spectra. Under the reaction conditions slightly more than half of the hydroxyl groups were

conjugated with CPT, giving a CPT content of 9.61wt%, probably due to the steric effect of the tethered PEG chains. To conjugate CPT to all the hydroxyl-groups to achieve the theoretical CPT content, 16.6 wt%, G_4-48acrylate was reacted with CPT-COOH first, and then reacted with PEG2k-SH for peripheral PEGylation. The resulting CPT content was17.4 wt%, because the PEGylation efficiency was about 91.5%.

2.2.3 Characterizations of G4-CPT-PEG

The G4-CPT-PEG with 9.61 wt% or 17.4 wt% CPT was very water soluble. Its average size in DI water was 22.5 or 24.2 nm, respectively. Thus, the PEGylated dendritic polymer with interior-conjugated CPT (G4-CPT-PEG) was unimolecular micelles with a core–shell structure. Compared to conventional micelles made from amphiphilic block copolymers, such drug-conjugated dendritic unimolecular micelles also have advantages of fixed drug loading without burst release, small micelle size, well-fined structure, and infinite stability. We compared the cytotoxicity of free CPT, G_4-PEG2k, and G_4-CPT-PEG (9.61 wt% CPT) to SKOV-3 ovarian cancer cells using the MTT assay. G_4-PEG2k was not toxic even at high doses. The IC_{50} of the CPT in the G_4-CPT-PEG to SKOV-3 cells was 0.499 μg/ml, slightly higher than that of free CPT (0.293 μg/ml), indicating that the CPT conjugated in the dendritic interior could be released inside cell.

2.2.4 Conclusion

We demonstrated a convenient synthesis of interior-and-peripheral-bifunctionalized dendritic polymers. These bifunctional dendritic polymers are nontoxic and biodegradable, offering a versatile platform for various biomedical applications. As a proof of a concept, the fourth-generation product was surface-pegylated with PEG2k and CPT was tethered in its interior, forming a core-shell dendritic polymer with a well-defined structure and a high drug loading capacity (~17.4 wt%). The new type dendritic polymer–drug conjugate behaved like a unimolecular micelle with good water solubility and stability. Thus, this conjugate is very promising as a drug delivery carrier.

2.3 Dendrimer/lipid nanoassembly as “cluster bomb” for cascade tumor penetration

Nanocarriers have been crafted to deliver anticancer agents to tumor tissues through passive accumulation (EPR effect) and active targeting (targeting ligands)[64, 65]. However, given the reduced adverse effects, the nanosystems do not show the high therapeutic efficacy that we expected[66, 67]. While many factors account for

this frustration, the nanosystems' limited penetration into the tumor and thus inaccessibility to the remote tumor cells may be an important determinant[68-70]. Tumors are characterized by unevenly distributed blood vessels—abundant at the invasive edge but few inside the tumor—and tightly packed cells in a dense extracellular matrix[71] with elevated interstitial fluid pressure[72, 73]. Thus, many regions in a tumor are far removed from blood vessels with limited diffusion of nano-sized carriers. Indeed, 100 nm-carriers were found to be restricted at the extravasation sites with little permeation into the tumor[74-76].

Smaller sized nanocarriers, e.g., about 30 nm or less in diameter, could better penetrate tumors[77], yet larger particles have proved to have slower blood clearance and thus longer blood circulation[78] and better tumor accumulation[77, 79, 80]. Furthermore, stealth nanocarriers are often equipped with targeting ligands that bind receptors on tumor cells or cationic charges to promote their cellular uptake[81]. However, such avid bindings strongly impede nanocarriers' tumor penetration[82]. Therefore, the design of tumor-penetrating nanocarriers must also simultaneously consider other properties including long blood circulation and fast cellular uptake to maximize therapeutic efficacy.

We proposed a long-circulating liposome that could release small nanocarriers capable of deep tumor penetration and fast tumor cell internalization uniting the essential elements of an ideal nanocarrier for cancer-drug delivery. Herein, we present such an example, a liposomal dendrimer nanoassembly (Scheme 6). The nanoassembly behaves like a cluster bomb capable of releasing smaller dendrimer nanocarriers (bomblets), uniting the large size needed for long blood circulation and the small size for tumor penetration and fast cellular uptake in the needed region.

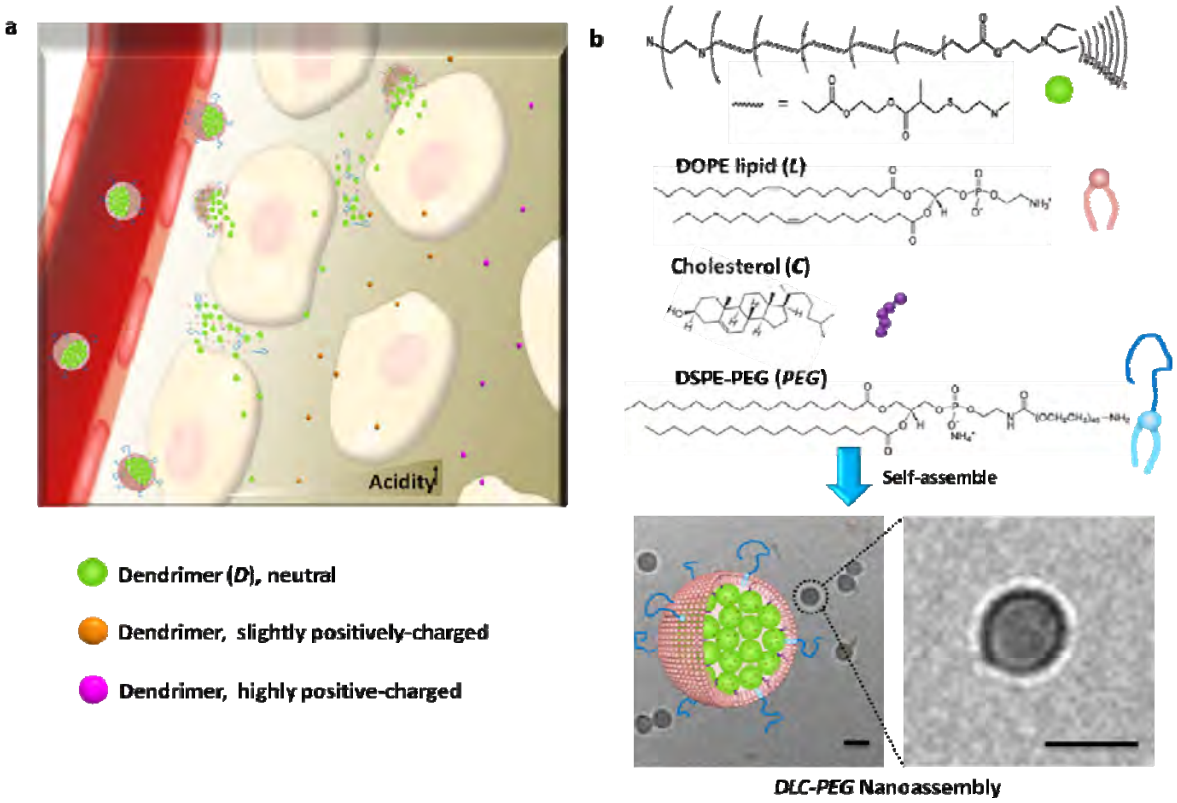

Scheme 6. Liposomal dendrimer nanoassembly (cluster bomb) concept uniting long blood circulation, deep tumor penetration, and fast cellular uptake (a) and the nanoassembly composition (b). a, The nanoassembly is a PEGylated liposome encapsulated with the dendrimer of several nanometers. It is stealthy and circulates in the blood compartment for tumor targeting via the EPR effect. After extravasating from the tumoral hyperpermeable blood vessels, the nanoassembly sheds its lipid layer and releases the dendrimer, which is small enough to penetrate deep into the tumor regions away from the blood vessels, where the pH is acidic and the dendrimer becomes positively charged for fast cellular uptake. b**,** The dendrimer was self-assembled with lipids and cholesterol to form the nanoassembly, which was confirmed by cryo-TEM image. The scale bar represents the length of 50 nm.

2.3.1 Preparation and characterization of the nanoassembly

The 6th-generation nontoxic, degradable polyaminoester dendrimer was synthesized as we previously synthesized[83]. Its diameter was about 5 nm. Its internal cavities were hydrophobic and hence could efficiently encapsulate hydrophobic anticancer drugs[84]. Furthermore, its periphery was functionalized with 2-(*N*,*N*-diethylamino)ethyl termini to render it pH dependence. Its zeta-potential was 3.2 mV at pH 7.4, 5.4 mV at pH 7.0 and 7.0 mV at pH 6.5. Hence, the dendrimer could be quickly internalized at acidic pH, thereby shipping drugs by bypassing the cell multidrug resistance. A phospholipid, 1,2-dioleoyl-sn-glycero-3-phosphoethanolamine (DOPE), chosen for its fusogenic characteristics,[85] was used for release of dendrimers within tumor. A PEGylated lipid, 1,2-distearoyl-*sn*-glycero-3-phosphoethanolamine-N-[amino(polyethylene

glycol)-2000] (DSPE-PEG), and cholesterol were added to give the nanoassembly stealth properties[86] and stability[87, 88] while in the blood compartment.

The self-assembly of the dendrimer (*D*) with DOPE lipid (*L*), cholesterol (*C*) and DSPE-PEG (*PEG*) was fine tuned in terms of the size, zeta-potential, and stability of the formed *DLC-PEG* nanoassembly (Figure 17). An optimal PEGylated *DLC* nanoassembly (*DLC-PEG*) was formed at a *D*/*L*/*C*/*PEG* molar ratio of 1/60/60/1.5 with a size of 30 ± 2 nm (PDI = 0.163) and a zeta-potential of –9.1 ± 0.5 mV. In 10 wt% bovine serum albumin solution at 37 °C, the *DLC-PEG* was stable for a prolonged time while assemblies without the cholesterol and DSPE-PEG components quickly collapsed. The structure of the *DLC-PEG* nanoassembly was probed by cryo-TEM. As illustrated in Scheme 6, the cryo-TEM images showed a dim ring surrounding a bright core, indicating a hydrophobic core surrounded by a hydrophilic layer. Thus, the *DLC-PEG* nanoassembly was calculated to be about 20 dendrimers (5 nm in diameter) aggregating together coated with a lipid monolayer.

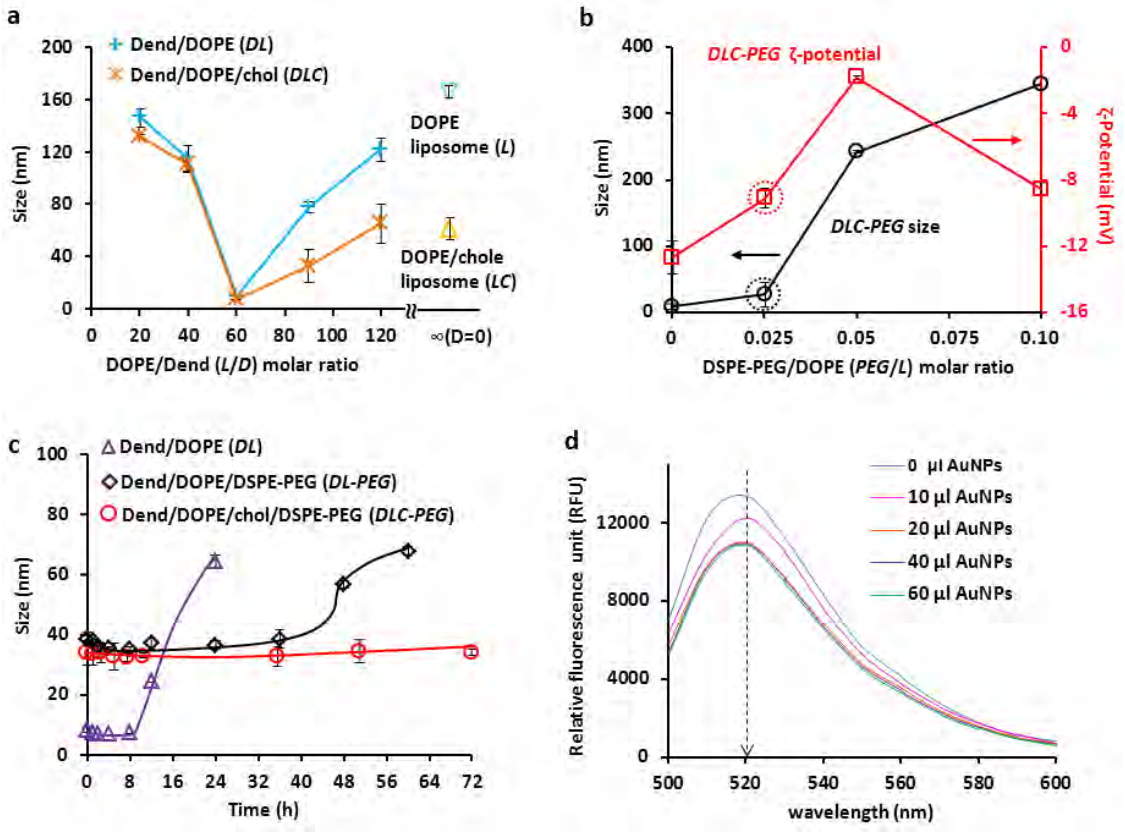

Figure 17. Self-assembly of the dendrimer and lipids into nanoassemblies and their characterizations. The concentration for all solutions was 1.2 mg dendrimer per milliliter. a, the size of the formed dendrimer/DOPE (Dend/DOPE, *DL*) nanoassembly as a function of DOPE/dendrimer (*L*/*D*) molar ratio with/without the addition of cholesterol (Chol or *C*) (*D*/*C* set at 1/60). b, The size and zeta-potential of *DLC-PEG* nanoassembly as a function of DSPE-PEG/DOPE (*PEG*/*L*) molar ratio (*D*/*L*/*C*=1/60/60). At DSPE-PEG 2.5 mol% DOPE lipid (i.e., the molar ratio D/L/C/PEG of 1/60/60/1.5), the *DLC-PEG* size was 30 ± 2 nm (PDI = 0.163) with a zeta-

potential of –9.1 ± 0.5 mV. c, The *in vitro* stability of nanoassemblies of the dendrimer/lipid (*DL)*, dendrimer/lipid/DSPE-PEG *(DL-PEG)* and dendrimer/lipid/cholesterol/DSPE-PEG (*DLC-PEG)* examined by monitoring their sizes over time in 10 wt% BSA solution at 37 °C (triplicate data). d, FITC fluorescence quenching method probing the lipid layer of the nanoassembly *DLC-PEG*. The dendrimer was labeled with FITC and used to prepare the labeled nanoassembly ^{FITC}*DLC-PEG* at 1.2 mg dendrimer/ml; gold nanoparticles (4 nm, 1 mg/ml) were added to the solution and the FITC fluorescence was recorded.

The nanoassembly structure was further probed using a fluorescence quenching approach[89]. A fluorescence dye, FITC, was tethered to the dendrimer (^{FITC}dendrimer or ^{FITC}*D*), and the ^{FITC}dendrimer was used to fabricate the labeled nanoassembly, ^{FITC}*DLC-PEG*. The FITC fluorescence peak at 530 nm in free ^{FITC}dendrimer shifted to 520 nm after it assembled into ^{FITC}*DLC-PEG* due to the hydrophobic environment. Gold nanoparticles (AuNPs, 4 nm) are known to quench the fluorescence of FITC and are of a size that cannot diffuse though a lipid layer. Thus, in solution the fluorescence of ^{FITC}dendrimer was gradually quenched upon adding AuNPs. However, adding AuNPs to the ^{FITC}*DLC-PEG* nanoassembly solution only slightly reduced the fluorescence intensity (Figure 17d). This suggests that some free ^{FITC}dendrimer molecules were in the solution and quenched by AuNPs, but most of them were inaccessible to the 4 nm AuNPs, confirming that a lipid layer capsulated most ^{FITC}dendrimer molecules. We calculated the percentage of dendrimer encapsulated in *DLC-PEG* nanoassembly to be 82%.

2.3.2 Drug delivery by dendrimer/lipid nanoassembly

DOX employed as a model drug was loaded into the dendrimer in the *DLC-PEG* nanoassembly by first loading DOX into the dendrimer and using the dendrimer/DOX to fabricate the nanoassembly. The resulting DOX-loaded *DLC-PEG* (*DLC-PEG*/DOX) had a slightly larger diameter, 45 ± 5 nm and a DOX loading content of 9 ± 2 wt%. DOX slowly released from *DLC-PEG* indicating that the dendrimer and lipid synergistically suppressed burst release. The cellular uptake of *DLC-PEG* into SKOV-3 ovarian cancer cells was observed using confocal microscopy. The dendrimer was labeled with FITC and its fluorescence was assigned green; some DOPE was labeled with rhodamine (RHoB) and its fluorescence was assigned red. Thus, the dual-labeled nanoassembly, ^{FITC}*D*^{RHoB}*LC-PEG,* was seen as yellow spots. As illustrated in Figure 18a, after ^{FITC}*D*^{RHoB}*LC-PEG* was incubated with cells for 4 h, the dendrimer, lipid, and the nanoassembly (yellow spots) were attached on the cell membrane. After 12 h, the lipid was still on the cell membrane while the dendrimer

was found inside the cells, suggesting that the nanoassembly dissociated and released the dendrimer. Furthermore, the DOX delivered by the *DLC-PEG* nanoassembly was internalized into cells after 12 h incubation. Notably, dendrimers/DOX (red signal) delivered were not localized in the lysosomes (green signal; Figure 18b), but in the cytosol. This suggests that the dendrimers might not be internalized via the common endocytosis or macropinocytosis pathways. Thus, the effects of temperature and specific pathway inhibitors—chlorpromazine (an inhibitor of the clathrin-dependent pathway[90]), filipin (an inhibitor of the caveolae-dependent pathway[91]) and wortmannin (an inhibitor of the phosphatidylinositol 3-kinasespathway[92])—on the cellular uptake of the nanoassembly were probed using flow cytometry (Figure 18c). The cellular uptake was suppressed to some extent at low temperature (4 °C), suggesting the internalization was mainly energy dependent. The presence of chlorpromazine, filipin, or wortmannin had almost no effect on the cellular uptake of the dendrimer, indicating that the cellular uptake of the dendrimers in the assembly was not through the common endocytosis or macropinocytosis pathways.

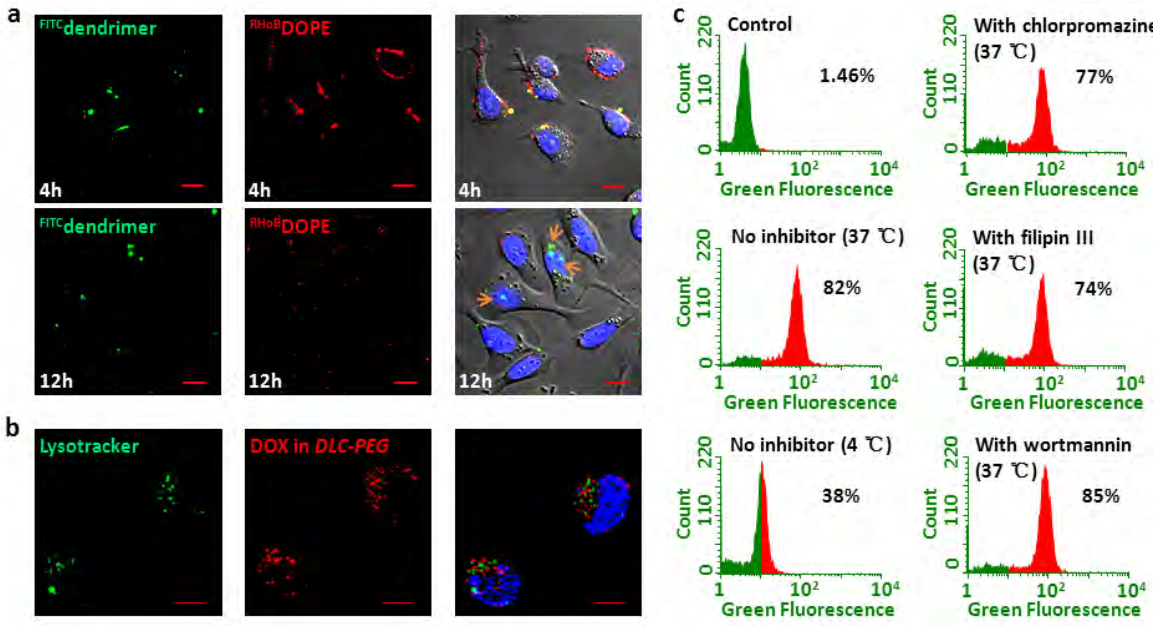

Figure 18. Cell interaction and disassociation (a), intracellular localization (b), and internalization (c) of the nanoassembly. a, Cellular uptake of *DLC-PEG* by SKOV-3 cells observed. The cells were treated with dual-labeled $^{FITC}D^{RHoB}LC$-*PEG* nanoassembly for 4 and 12 h, respectively. The FITC-equivalent dose was 60 μg/ml. ^{FITC}dendrimer is shown in green; ^{RHoB}DOPE is shown in red; cell nuclei were stained with Draq 5 in blue. All scale bars were 10 μm. b, Subcellular localization of *DLC-PEG*/DOX. The SKOV-3 cells were treated with *DLC-PEG*/DOX at a DOX-equivalent dose of 0.8 μg/ml for 6 h. Lysotracker dyed lysosomes shown in green; DOX loaded in *DLC-PEG* shown in red. All scale bars were 10 μm. c, The FITC-positive SKOV-3 cells after treatment with ^{FITC}*DLC-PEG* for 6 h at different temperatures or at 37 °C in the presence of chlorpromazine, filipin or wortmannin. The FITC-equivalent dose was 60 μg/ml.

We used a fluorescence-resonance energy-transfer (FRET) approach[93, 94] to probe the fusion of the lipid layer with the cell membrane. Two FRET fluorescent dyes, RHoB and NBD, were separately tethered to the DOPE lipid (^{RHoB}DOPE and ^{NBD}DOPE). They were mixed with DOPE at a DOPE/^{RHoB}DOPE/^{NBD}DOPE molar ratio of 94/1/5 and used to form the lipid-dually labeled nanoassembly, $D^{RHoB/NBD}$*LC-PEG* (Figure 19a). A FRET efficiency index, *R*, can be calculated from the intensity ratio of ^{RHoB}DOPE fluorescence at 585 nm to the ^{NBD}DOPE fluorescence at 525 nm excited at 450 nm[93]. Upon excitation at 450 nm, the intact $D^{RHoB/NBD}$*LC-PEG* nanoassembly had a strong FRET-fluorescence peak at 585 nm and a weak peak at 525 nm with an *R* value of 3.4. As a control experiment, adding 0.24 vol% Triton X-100 to dissolve and dissemble the nanoassembly completely eliminated the FRET. The treated cells, which were treated with $D^{RHoB/NBD}$*LC-PEG* nanoassembly PBS-CM solution for 6 h and then isolated and resuspended in fresh PBS-CM solution, had a weak FRET with an *R* value of 0.39, indicating the fusion of the lipid layer with the cell membrane.

To test the extracellular dendrimer release, we incubated ^{FITC}*DLC-PEG* with SKOV-3 cells in PBS-CM solution at 37 °C for different times and then collected the extracellular nanoassembly solutions. The ^{FITC}dendrimer fluorescence was measured and the nanoassembly integrity was probed again using the AuNP quenching method (Figure 4b). After the nanoassembly was incubated with the cells for 5 min, some ^{FITC}dendrimer fluorescence became quenchable by AuNPs, and the peak FITC emission shifted from 520 nm to 530 nm, typical for FITC in a hydrophilic environment. This phenomenon became much more pronounced after longer incubation. After 45 min incubation, the ^{FITC}dendrimer fluorescence could be completely quenched after adding 100 μl of the AuNP solution, which was very similar to that of the free ^{FITC}dendrimer, indicating that the dendrimers in the extracellular solution were mostly exposed to an aqueous environment.

Therefore, it can be concluded that the fusion of the nanoassembly lipid layer to the cell membrane stripped off its lipid layer and released dendrimers either into the cell cytosol or the extracellular medium. This triggering resolves the size dilemma between blood circulation and tumor penetration.

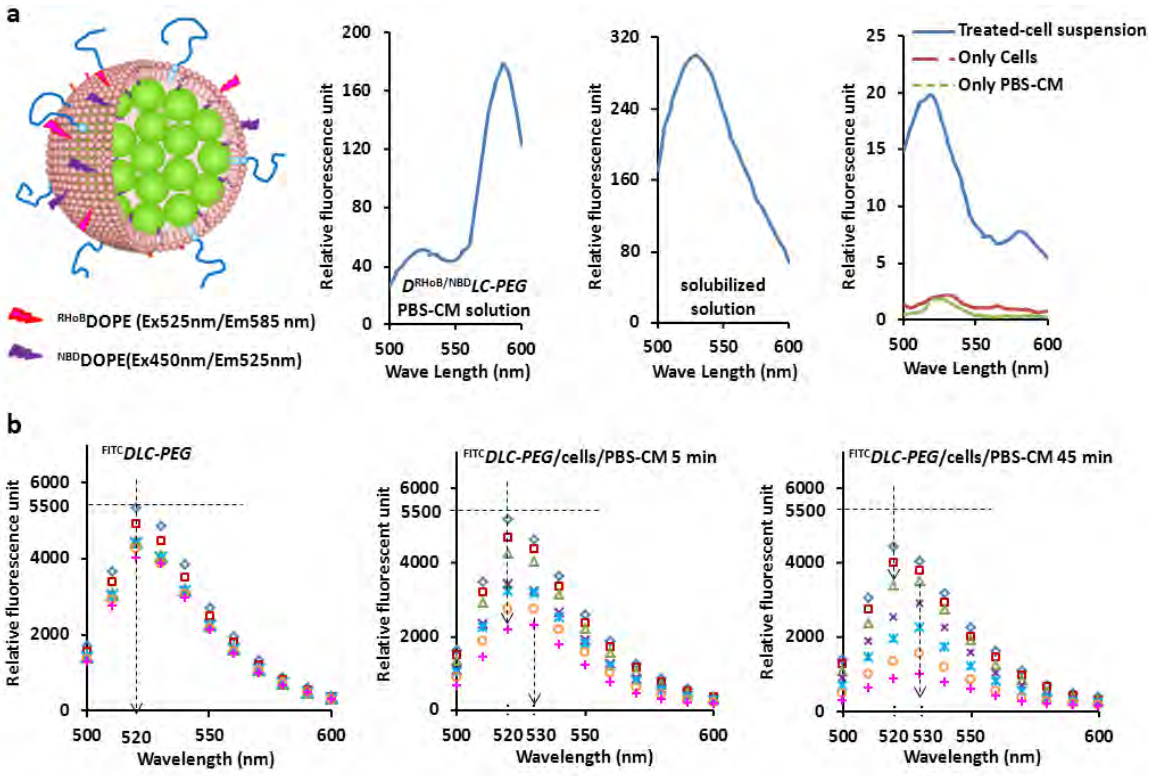

Figure 19. The fusion study of the *DLC-PEG* nanoassembly with the cell membrane (a) and its extracellular dendrimer release (b). a, Fusion assay using a fluorescence-resonance energy-transfer (FRET) approach. The *DLC-PEG* lipid layer was dual labeled with ^{NBD}DOPE (ex 450 nm/em 525 nm) and ^{RHoB}DOPE (ex 525 nm/em 585 nm) at a DOPE/^{RHoB}DOPE/^{NBD}DOPE molar ratio of 94/1/5. All the fluorescence emission spectra were recorded excited by a 450 nm laser. **b,** Dendrimer released into extracellular medium from *DLC-PEG* induced by fusion. The FITC fluorescence of the solution was measured before and after adding different amounts of gold nanoparticles (AuNPs; 1 mg/ml; before quenching, diamond; 10 µl AuNPs, square; 20 µl, triangle; 40 µl, X; 60 µl, asterisk; 80 µl, circle; 100 µl, cross).

2.3.3 In vitro and in vivo administrations of the nanoassembly

The cytotoxicity of DOX loaded in *DLC-PEG* (*DLC-PEG*/DOX) to three cancer cell lines, MDA-MB-468 and BCAP-37 breast cancer cells and SKOV-3 ovarian cancer cells, was slightly lower than that of free DOX. The blank *DLC-PEG* had no cytotoxicity.

The *in vivo* stealth properties of *DLC-PEG* were compared with standard PCL-PEG micelles. Both the nanoassembly's dendrimer and the PCL-PEG (the PCL end) were conjugated with FITC for nonleaching labeling. A hydrophobic fluorescence probe, DiR, was loaded instead of DOX into the ^{FITC}*DLC-PEG* nanoassembly and the ^{FITC}PCL-PEG micelles for tracing because the fluorescence wavelengths of DOX and FITC are partially overlapped. The *DLC-PEG*/DiR (45 nm in diameter) was found to have a blood circulation similar to that of the well-known long-circulating $PCL_{2.5k}$-PEG_{5k}/DiR micelles, suggesting that the nanoassembly indeed had good stealth properties (Figure 20a). The biodistribution profile in organs responsible

for clearance (liver, spleen, kidneys) showed no statistical difference at 16 h post-injection. However, *DLC-PEG*/DiR accumulated more in SKOV-3 xenografted tumor than $PCL_{2.5k}$-PEG_{5k}/DiR as calculated by the overall fluorescence intensity of either FITC labeled carriers or the loaded DiR dye in the tumor cells. The ^{FITC}dendrimer accumulated in tumor was 1.7 (p = 0.038) times of FITC-labeled $PCL_{2.5k}$-PEG_{5k}; similarly, DiR-loaded *DLC-PEG* accumulated in the tumor was 1.5 times of the DiR-loaded $PCL_{2.5k}$-PEG_{5k} (Figure 20b).

The dual-labeled $^{FITC}D^{RHoB}$*LC-PEG* nanoassembly was loaded with a model drug DiR ($^{FITC}D^{RHoB}$*LC-PEG*/DiR) and used to observe the intratumoral distribution, nanoassembly dissociation, and drug release using confocal microscopy. Figure 20c shows a representative part of a solid tumor slice (10 μm thick) excised from SKOV-3 tumor-bearing mice at 16 h post-injection with $^{FITC}D^{RHoB}$*LC-PEG*/DiR. The ^{FITC}dendrimer (green signal) was separate from the ^{RHoB}DOPE (red signal), suggesting the dissociation of the dendrimers and lipid layer in the tumor. In Figure 20d, the green signal of the ^{FITC}dendrimer and the red signal of DiR are mostly overlapped as yellow spots after the nanoassembly extravasated from the blood vessel into the tumor (magnified area 1), and they still overlapped during deep penetration through the tumor tissue (magnified area 2), indicating that the dendrimer retained the DiR well. Furthermore, the dendrimer was distributed throughout the tumor. In contrast, a relatively small number of the 75 nm $PCL_{2.5k}$-PEG_{5k} appeared mostly at the invasive edges and very few appeared inside the tumor, where it released the DiR. This indicates that the nanoassembly could circulate longer in the bloodstream and efficiently accumulat in the tumor. Once in the tumor, the nanoassembly shed the lipid layer and released the dendrimer; the dendrimer carried the loaded drug (DiR here), penetrating and distributing throughout the whole tumor.

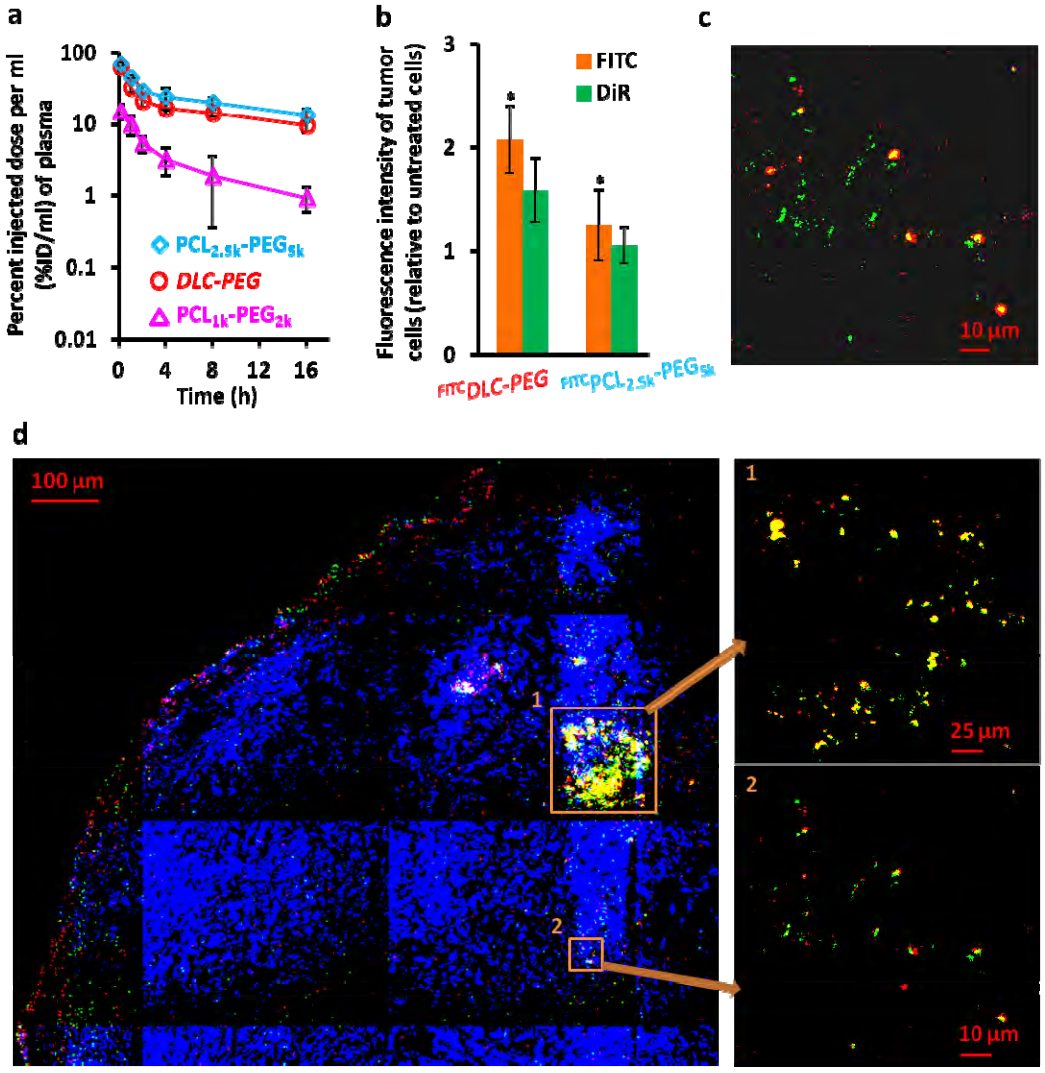

Figure 20. *In vivo* blood clearance (a), tumor accumulation (b), disassociation (c), and tumor distribution (d) of *DLC-PEG* nanoassembly. a, Blood clearance of DiR loaded *DLC-PEG* nanoassembly (45 nm in diameter), $PCL_{2.5k}$-PEG_{5k} (75 nm) and PCL_{1k}-PEG_{2k} (25 nm) nanoparticles in female athymic mice after a single dose of 0.15 mg DiR/kg body weight. b, The accumulation of DiR-loaded ^{FITC}*DLC-PEG* nanoassembly and $^{FITC}PCL_{2.5k}$-PEG_{5k} nanoparticles in tumors is calculated in terms of fluorescence intensity of tumor cells. c, d, The dissociation and the intratumoral distribution of DiR-loaded ^{FITC}dendrimer- and ^{RHoB}DOPE-labeled nanoassembly ($^{FITC}D^{RHoB}LC$-*PEG*/DiR) in SKOV-3 tumor tissue.

We further examined the tumor accumulation and penetration of the real drug DOX delivered by *DLC-PEG* in BCAP-37 tumor-bearing mice and compared them with similar-sized PCL_{2k}-PEG_{2k}/DOX nanoparticles (40 nm in diameter). The *DLC-PEG* delivered 1.7 (p = 0.024) times as much DOX as was delivered by PCL_{2k}-PEG_{2k} at 16 h post-injection (Figure 21a). The confocal image of a tumor slice (10 μm thick) sectioned from the tumor treated with *DLC-PEG*/DOX clearly had DOX much more homogeneously distributed in the tumor, whereas the DOX delivered by PCL_{2k}-PEG_{2k} was mostly retained in the invasive edge (Figure 21b & c). This further proves that the nanoassembly *DLC-PEG* could release the dendrimers once in the tumor by stripping off

the lipid layer, and the small dendrimer could penetrate more deeply into the whole tumor tissue, which is advantageous over conventional fixed-size nanoparticles.

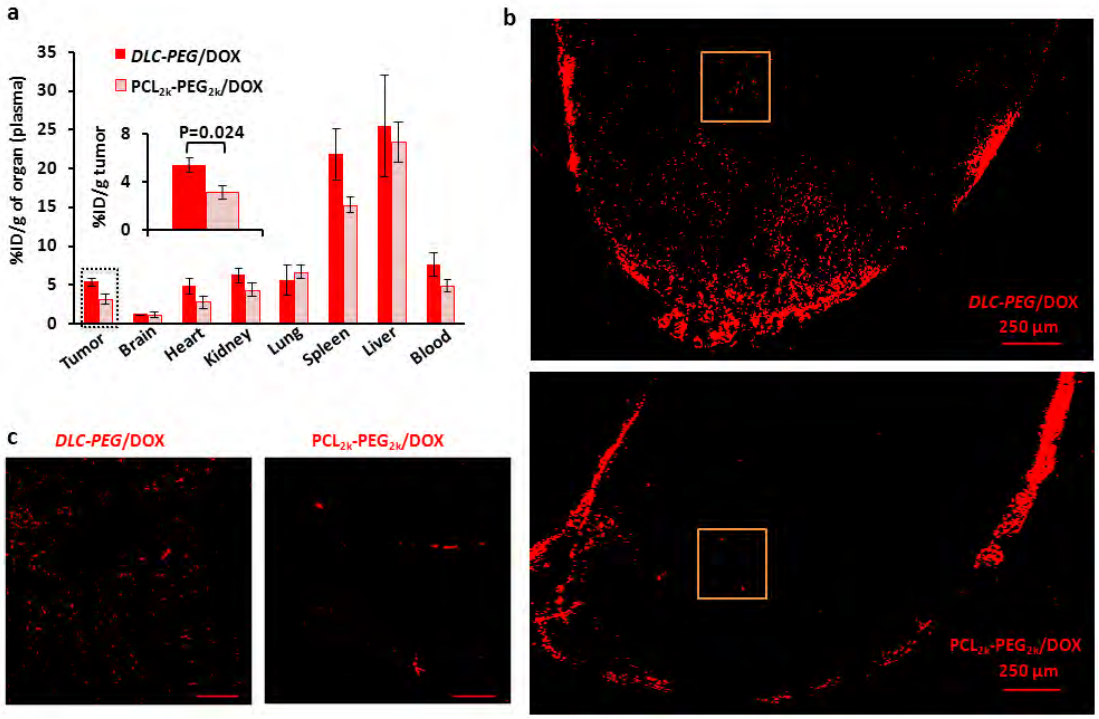

Figure 21. DOX Biodistributions and intratumoral distributions of *DLC-PEG*/DOX and its control PCL_{2k}-PEG_{2k}/DOX. a, Biodistributions of *DLC-PEG*/DOX (45 nm) and PCL_{2k}-PEG_{2k}/DOX (40 nm) in BCAP-37 tumor-bearing mice 16 h after a single injection of 1 mg DOX/kg body weight. b, The representative confocal images obtained under tile scanning of the complete tumor tissue slides (10 μm thick, a half of the whole slides) sectioned from the BCAP-37 tumors. DOX is shown in red. The magnified views of the selected areas in (b) are shown in c. The scale bar is 50 μm.

2.3.4 Conclusion

We have demonstrated that the dendrimer/lipid (*DLC-PEG*) nanoassembly can improve tumor accumulation, penetration, and cellular uptake. The nanoassembly behaves like a “cluster bomb”: it circulates in the blood compartment for a long period, efficiently accumulates in a tumor, and subsequently sheds off the lipid layer to release the small dendrimers carrying drugs (bomblets) to penetrate the tight tumor tissue. The released pH-sensitive dendrimers shepherded the drugs past the multidrug resistance and were quickly internalized by the cells. The “cluster bomb” concept may be a very promising approach uniting the needed properties for high chemotherapeutic efficacy.

3. Novel nanorods as carriers for drug delivery

Prolonging the nanocarrier’s blood circulation time increases its opportunity to pass through the leaky

vasculature, and thereby its extravagation into the tumor tissue[95]. Surface properties and size of a nanocarrier are the two important factors affecting its blood circulation time[96-100]. Besides, the nanocarrier shape has been recognized as another important parameter strongly affecting its circulation time[101-106].

PEGylated metallic and inorganic nanorods[107, 108] as models were demonstrated to long circulate like wormlike micelles[101-103] and have the ability to penetrate tumor efficiently via the enhanced pore transportation[109] and fast cellular uptake[110-112] compared to nanospheres; however, they cannot be used in clinics for intravenous drug delivery. Unfortunately, amphiphilic copolymers form rod-like morphology only within very narrow composition ranges depending on the polymer natures[113, 114]

Herein, we report a self-assembly of well-defined linear-dendritic conjugates, PEG–*block*-dendritic polylysine-camptothecin (PEG-xCPT), into rod-like nanocarriers characteristic of biodegradability, high drug loading contents free of burst release, long blood circulating, fast cellular internalization, and intracellular drug release (Scheme 7).

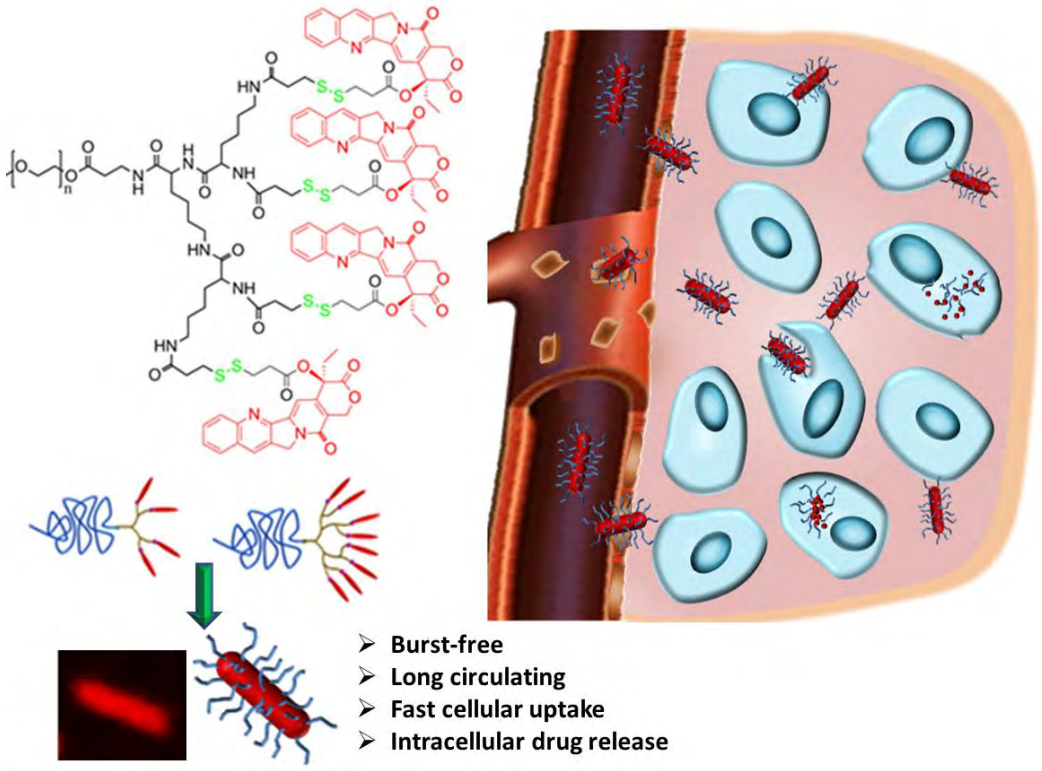

Scheme 7. Self-assembly of PEG_{45}-dendritic polylysine-camptothecin (PEG-xCPT) conjugates into biodegradable nanospheres or nanorods with high drug loading: The formation of the morphologies was determined by the generation of the dendritic polylysine and the number of the conjugated CPT. Nanorods with short length (< 500 nm) have characteristics of long blood circulating, fast cellular internalization, and intracellular drug release.

3.1 Synthesis of PEG-xCPT conjugates

The CPT-PDP containing a disulfide bond and an *NHS* active ester group was first synthesized. PEG-*block*-dendritc PLL (DPLL) of different generations was prepared and then reacted with a corresponding amount of CPT-PDP to obtain PEG-DPLL conjugated with 1, 2, 4 or 8 CPT molecules. The structures of the conjugates PEG-xCPT as shown in Scheme 7 were characterized by MALDI-TOF MS spectra, ^{1}H NMR spectra, HPLC and GPC. Table 2 summarizes the characterizations and the properties of these conjugates. Notably, the CPT contents of PEG_{45}-CPT, PEG_{45}-DiCPT, PEG_{45}-TetraCPT and PEG_{45}-OctaCPT were 13.4%, 21.4%, 30.6% and 38.9% by weight, respectively.

Table 2. Summary of the characterizations and properties of PEG-DPLL-CPT conjugates.

PEG-DCPT	Mn		CPT content[b]	PEG content[b]	Morphology	IC_{50} (μg/mL)		PK parameters	
	Cal.	found[a]				24 h	72 h	AUC (%IDh/g)	$t_{1/2}$ (h)
PEG_{45}-CPT	2593	2605	13.4%	77.1%	sphere	0.64	0.083	-	-
PEG_{45}-DiCPT	3243	3215	21.4%	61.7%	sphere	0.82	0.0088	47.13	1.61
PEG_{45}-TetraCPT	4543	4386	30.6%	44.0%	rod	6.34	0.049	239.71	5.82
PEG_{45}-OctaCPT	7143	6853	38.9%	28.0%	rod	6.45	0.081	58.2	1.70

3.2 Preparation and characterization of the nanorod

The PEG-xCPT formed nanoparticles at concentrations higher than their CMCs. The morphologies of the nanoparticles in the aqueous solution were observed using TEM (Figure 22 A-C). PEG_{45}-CPT and PEG_{45}-DiCPT (Figure 22 A) formed uniform ~100 nm nanospheres. Interestingly, PEG_{45}-TetraCPT and PEG_{45}-OctaCPT formed unusual nanorods (Figure 22, B and C). The nanorods of PEG_{45}-TetraCPT were about 60 nm in diameter and 500 nm long, and those of PEG_{45}-OctaCPT were about 100 nm in diameter and about one micrometer long. These structures were further confirmed by confocal fluorescence microscopy after loaded with a fluorescent dye nile red (Figure 22 D-E).

The stability study of the nanostructures showed the PEG_{45}-DiCPT nanospheres and PEG_{45}-TetraCPT nanorods were stable over 5 days and their sizes did not change over the time, while PEG_{45}-OctaCPT nanorods

slightly aggregated. All these nanospheres or nanorods did not release any CPT in PBS at 37 °C. However, in the presence of DTT, the nanospheres or nanorods immediately released CPT-SH as detected by HPLC.

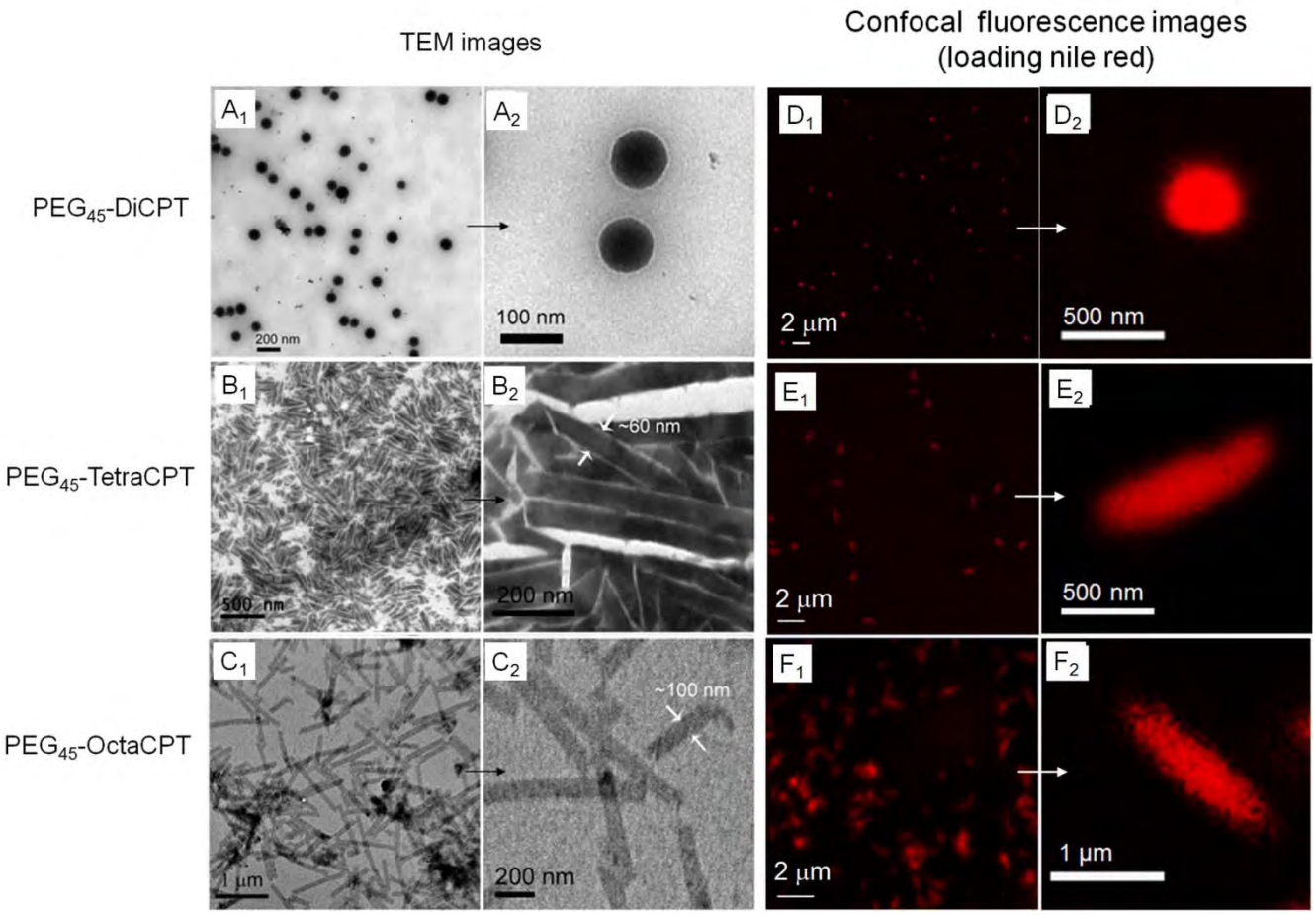

Figure 22. The TEM images of PEG_{45}-DiCPT (A), PEG_{45}-TetraCPT (B), PEG_{45}-OctaCPT (C) nanostructures and the confocal florescence images of PEG_{45}-DiCPT (D), PEG_{45}-TetraCPT (E) and PEG_{45}-OctaCPT (F) nanostructures loaded with Nile red and their corresponding enlarged images.

3.3 Drug delivery by the nanorod

DOX was loaded as a tracer to the nanocarriers (PEG_{45}-DiCPT/DOX) and nanorods (PEG_{45}-TetraCPT/DOX and PEG_{45}-OctaCPT/DOX) for cell internalization study using confocal microscopy and flow cytometry (Figure 23). As shown in Figure 23A, the cellular uptakes of DOX-loaded nanospheres or nanorods were different from that of free DOX. Free DOX easily entered the non-drug-resistant cells (MCF-7) by passive diffusion, as evidenced by the strong fluorescence in whole cells; only very weak DOX fluorescence was observed in multidrug-resistant cells (MCF-7/ADR) since DOX is a substrate of their drug resistance. In contrast, strong DOX fluorescence was observed in both MCF-7 and MCF-7/ADR cells after they were cultured with DOX-loaded nanoparticles for one hour, and the intracellular fluorescent intensity increased gradually with

prolonging the culturing time (4 or 8 h). Two more phenomena were further observed: In MCF-7 cells, the intracellular DOX distributed in the whole cells after 8 h culture, including the nuclei; but in MCF-7/ADR cells, the intracellular DOX could not enter the nuclei. Furthermore, the DOX-intensity of the cells cultured with the nanorods (PEG_{45}-TetraCPT/DOX and PEG_{45}-OctaCPT/DOX) was much higher than those cultured with the nanospheres (PEG_{45}-DiCPT/DOX), particularly those with the PEG_{45}-OctaCPT/DOX nanorods, suggesting much faster cellular uptake of the nanorods than that of the nanospheres. This was further proven by quantitation using by flow cytometry (Figure 23B) in terms of the fold increase of the mean fluorescence intensity relative to control. Clearly, at each time points, the cells cultured with nanorods PEG_{45}-TetraCPT/DOX or PEG_{45}-OctaCPT/DOX had higher fluorescent intensities than that of those cultured with the spherical PEG_{45}-DiCPT/DOX (all $P<0.01$). At 8 h culture, the DOX intensity of the cells cultured with PEG_{45}-TetraCPT/DOX or PEG_{45}-OctaCPT/DOX was 1.15 or 1.39 fold of those cultured with PEG_{45}-DiCPT/DOX.

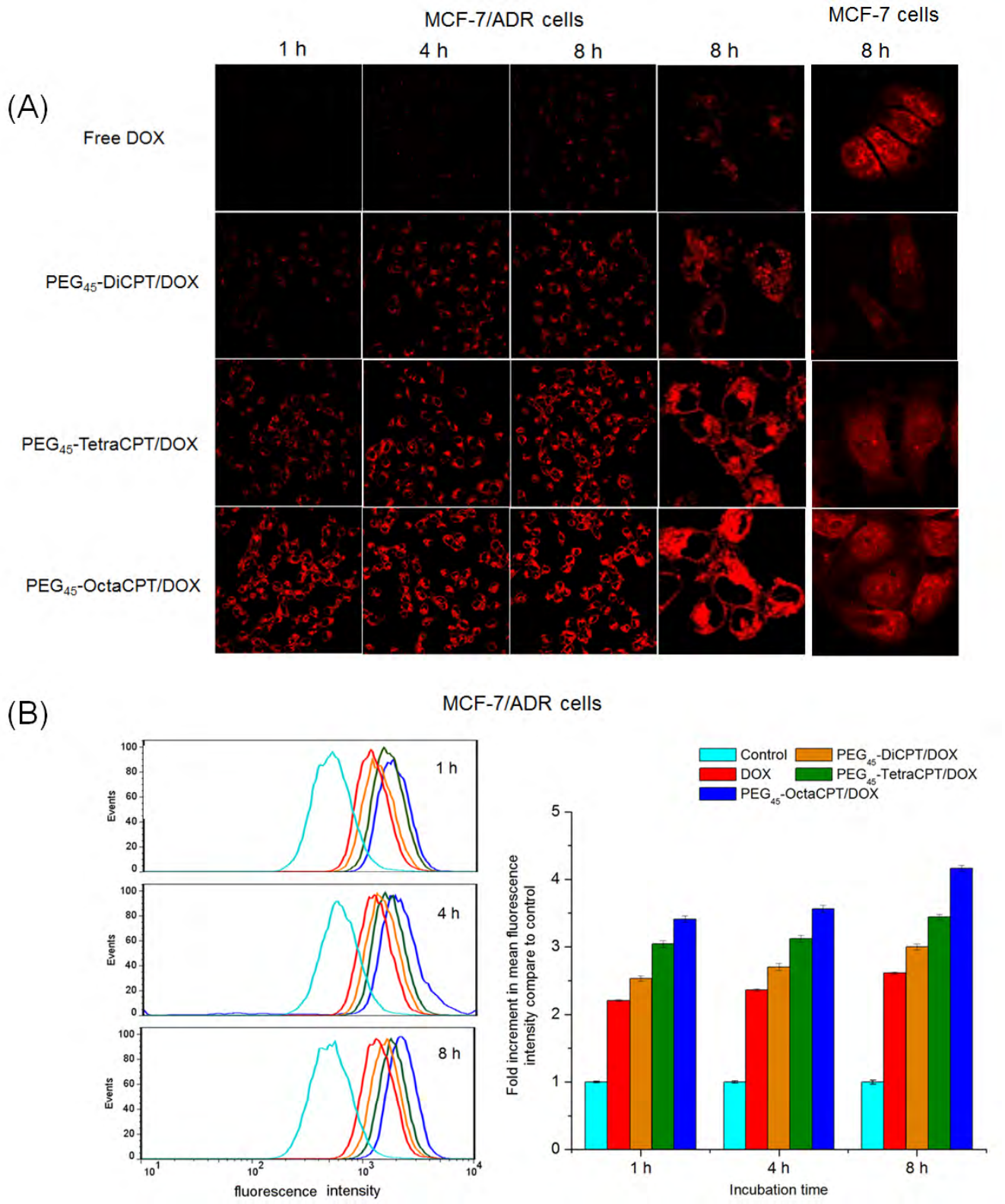

Figure 23. Cellular uptake study of free DOX, PEG_{45}-DiCPT/DOX, PEG_{45}-TetraCPT/DOX and PEG_{45}-OctaCPT/DOX by confocal microscopy (A) and flow cytometry (B). The free DOX and the DOX-loaded nanostructures (DOX dose: 4 μg/mL) were cultured individually with MCF-7 or MCF-7/ADR cancer cells at 37 ^{o}C for 1, 4 or 8 hours.

3.4 In vitro and in vivo administrations of the nanorod

The cytotoxicity of free CPT, and the nanospheres/nanorods to MCF-7 or MCF-7/ADR cancer cells was evaluated using the MTT assay. With 72 h culture, the IC_{50} value to MCF-7 cells was 0.138 μg/mL for PEG_{45}-DiCPT, 0.073 μg/mL for PEG_{45}-TetraCPT and 0.070 μg/mL for PEG_{45}-OctaCPT, higher than that of CPT.

The pharmacokinetics and biodistribution of nanospheres and nanorods were studied after *iv* administration to BALB/c mice. Figure 24A shows the blood clearance profiles. Less than 1% of the injected free CPT was reported to remain in the blood after 30 min[115]. The nanospheres or nanorods had much prolonged blood circulation times than CPT, but PEG_{45}-TetraCPT nanorods had the longest blood circulation time. Elimination half-lives ($t_{1/2, \beta}$) were calculated using a two-compartment model (Table 2). Thus, PEG_{45}-TetraCPT nanorods had a much better stealth property than the PEG_{45}-DiCPT nanospheres, suggesting that nanorods more effectively resisted opsonization or nonspecific binding of proteins and avoided RES clearance.

The biodistributions of the nanocarriers in terms of CPT concentration in different organs of mice at 4 and 24 h post *iv* administration are shown in Figures 24 B and C. At 4 h, spleen was the major organ sequestering the nanocarriers for all three systems. Thus, the spleen was still responsible for the clearance of the nanospheres and nanorods. Clearly, PEG_{45}-TetraCPT had lower concentrations in liver and spleen than PEG_{45}-DiCPT, consistent with the results in Figure 24 A. After 24 h, PEG_{45}-DiCPT almost disappeared from all the organs. PEG_{45}-TetraCPT was still found in the spleen (22.05 ± 6.33% ID/g tissue) and blood (3.59 ± 0.29 % ID/g blood).

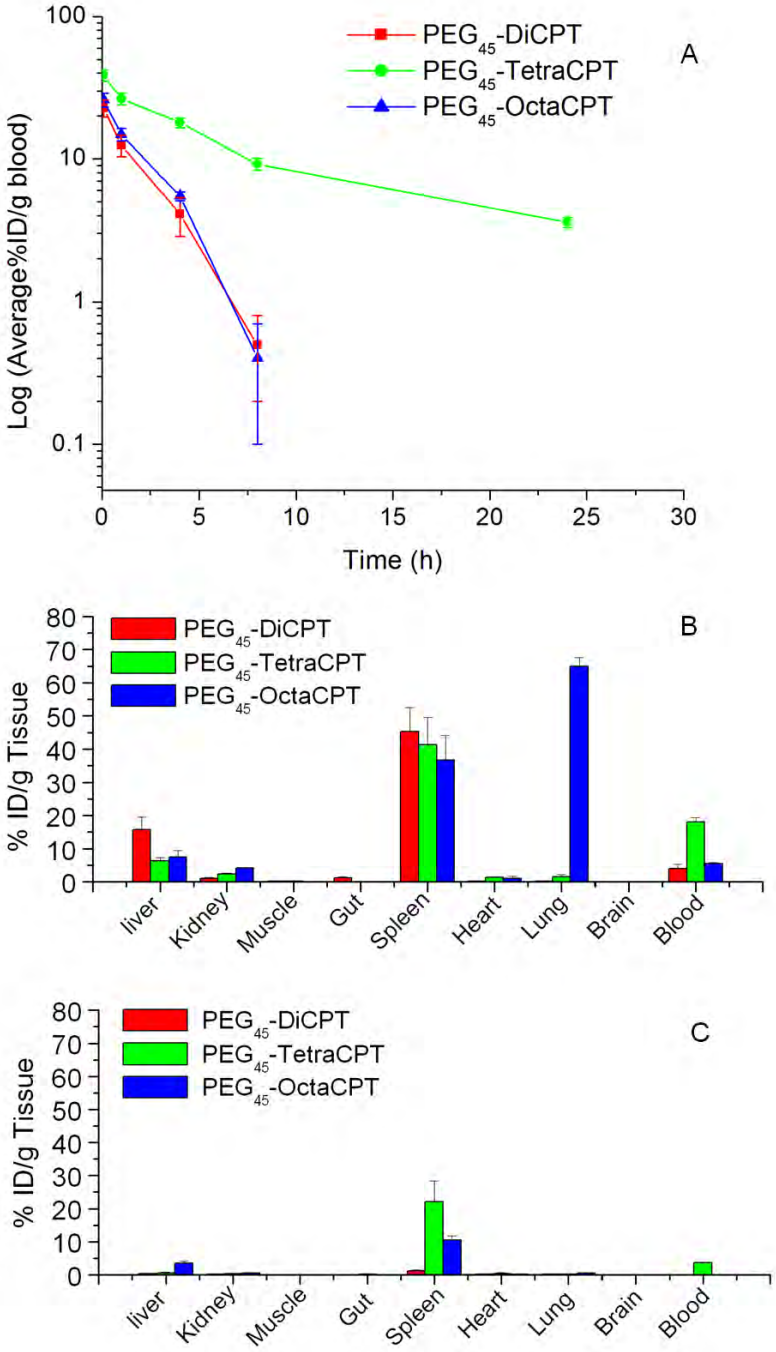

Figure 24. Blood clearance profiles of PEG_{45}-xCPT given in percent of the injected dose per gram of the blood (% ID/g blood) (A), and their biodistributions given in % ID/g of tissue collected at 4 (B) or 24 h (C) after injection.

Ex vivo imaging of excised tissues and tumors at 8 h post-injection showed an obvious tumor accumulation of the DOX-loaded nanoparticles (Figure 25). The mice injected with PEG_{45}-DiCPT/DOX or PEG_{45}-OctaCPT/DOX had higher DOX fluorescence in liver than that injected with PEG_{45}-TetraCPT/DOX. The mouse injected with PEG_{45}-OctaCPT/DOX had higher DOX fluorescence in lung than those injected with other nanoparticles. Very low fluorescence was observed in heart and spleen for all the mice. Side-by-side

comparison of the tumors from mice injected with PEG_{45}-DiCPT/DOX or PEG_{45}-TetraCPT/DOX is shown in Figure 25C. Fluorescence intensity in tumors of the mice injected with PEG_{45}-TetraCPT/DOX was 2.8 times of those injected with PEG_{45}-DiCPT/DOX. The t-student test indicated the DOX fluorescence in the tumors from mice injected with nanospheres and nanorods was statistically different.

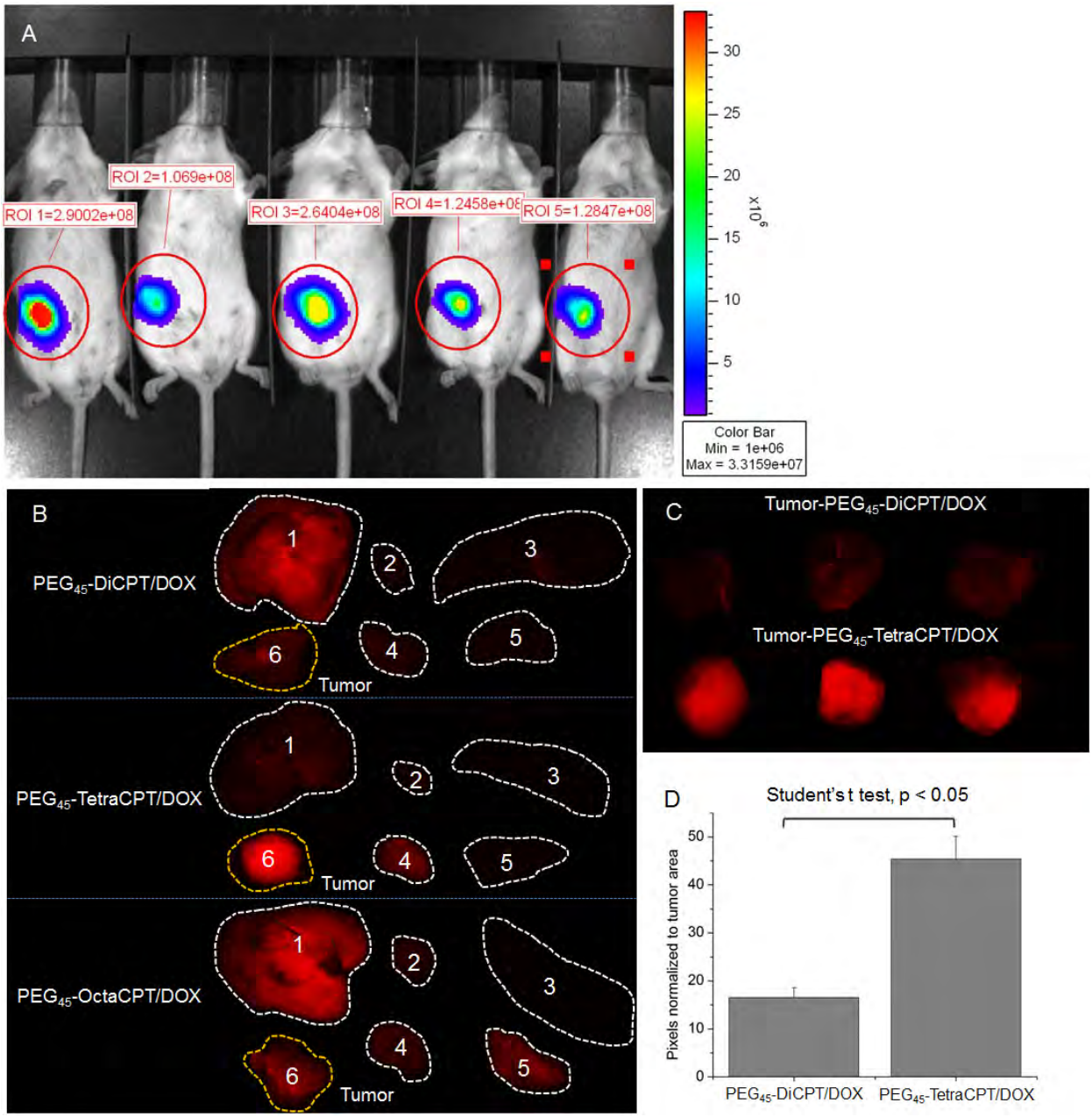

Figure 25. (A) Bioluminescence images showing mice bearing 4T1-Luc breast tumor in mammary fat pad two weeks after implant. Mice were intraperitoneal injected with D-luciferin (150 mg/kg body weight) 10 min before imaging with Xenogen IVIS Lumina system. (B) Mice bearing 4T1-Luc breast tumor were intravenously injected with DOX-loaded nanoparticles (5 mg DOX-equivalent/kg body weight). After 8 h, the mice were sacrificed and the tumors and various organs (1. Liver, 2. Heart, 3. Spleen, 4. Kidney, 5. Lung, 6. Tumor) were imaged with the Maestro FLEX In Vivo Imaging System. (C) Tumors of mice injected with PEG_{45}-DiCPT/DOX or PEG_{45}-TetraCPT/DOX were imaged side by side with the Maestro FLEX *In Vivo* Imaging System and (D) the pixels normalized to tumor area analyzed with Maestro software.

3.5 Conclusion

We demonstrated a facile approach to fabricate polymer-drug conjugate nanorods for cancer-drug delivery. Using a hydrophobic drug as the hydrophobic moiety, well-defined amphiphilic linear-dendritic drug conjugates, PEG-b-dendritic polylysine-CPT, were synthesized. Tailoring their generation and the number of the conjugated CPT molecules induced the linear-dendritic conjugates to self-assemble into spherical or rod-like nanostructures stable at the physiological conditions but quickly releasing the drug CPT once in the cytosol. The shape of the nanostructures affected their cellular uptake and in vivo blood clearance. The nanorods were taken up more efficiently by cancer cells than nanospheres. The nanorods with medium lengths (<500 nm) also had a much better stealth property and thus a much longer blood circulation time than the nanospheres.

4. Review of translational nanocarriers for drug delivery

Cancer drug delivery is a process using nanocarriers with appropriate sizes (usually between several nanometers and 200 nm) and stealth properties to preferentially carry drugs to tumor tissues. However, despite the improved pharmacokinetic properties and the reduced adverse effects, currently cancer drug delivery has only achieved modest therapeutic benefits[116, 117]. Thus, design of nanocarriers with more efficient drug delivery and thus higher therapeutic efficacy is still a pressing need.

Therefore, we proposed a truly translational nanocarrier should firstly capable of simultaneously satisfying *2R2S* requirements, which is "drug *R*etention in blood circulation *vs. R*elease in tumor cells (*2R*)" and "surface *S*tealthy in blood circulation and tumor tissues vs. *S*ticky to tumor cells (*2S*)", to delivery drugs specifically at the right time and the right place[118]. Furthermore, while the 2*R*2*S* capability of a nanocarrier may render its resulting nanomedicine efficacy and safety potential for clinical translation, other two elements, the feasibility of the nanocarrier materials to be proved for use as excipients (referred to as material excipientability) and the ability to establish scaling up production processes for good manufacture processes (GMP) for the nanocarrier and its formulation with drug (nanomedicine) (referred to as process scale-up ability) are also indispensible for the nanomedicine truly translational from the benchtop to the bedside (Scheme 8)[118]. The challenge to develop truly translational nanocarriers and nanomedicine is to use less excipientable materials and simple processes of scale-up ability to produce nanocarriers with optimal *2R2S* capability. While the research aimed at proof of

concepts remains important, it is important to increasingly focus on comprehensive approaches or systems that include *all* the three key elements, as early as possible in the innovation chain to speed up developments of translational nanomedicine.

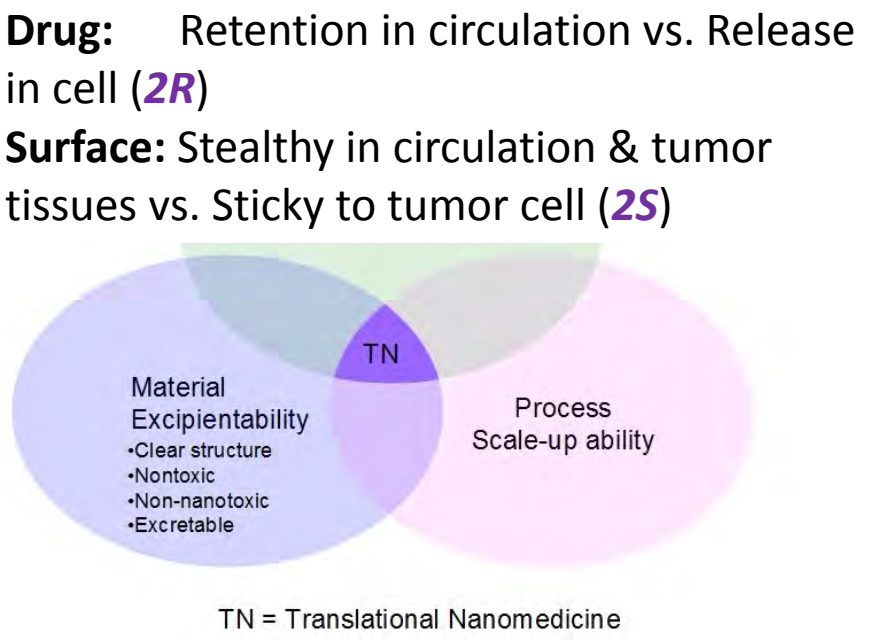

Scheme 8. The three elements for translational nanomedicine: the nanocarrier should have the 2*R*2*S* capability and its material should be suitable for excipient use (referred to as material excipientability); the production of the nanocarrier and its formulation with drug (nanomedicine) should be able to scale up for good manufacture process (GMP) (scale-up ability).

5. References

1. Manzoor Ashley, A.; Lindner Lars, H.; Landon Chelsea, D.; Park, J.-Y.; Simnick Andrew, J.; Dreher Matthew, R.; Das, S.; Hanna, G.; Park, W.; Chilkoti, A.; Koning Gerben, A.; Ten Hagen Timo, L. M.; Needham, D.; Dewhirst Mark, W. *Cancer Res.* **2012,** 72, (21), 5566-5575.
2. Zhu, L.; Kate, P.; Torchilin, V. P. *ACS Nano* **2012,** 6, (4), 3491-3498.
3. Soenen, S. J. H.; Brisson, A. R.; De Cuyper, M. *Biomaterials* **2009,** 30, (22), 3691-3701.
4. Yoshida, T.; Oide, N.; Sakamoto, T.; Yotsumoto, S.; Negishi, Y.; Tsuchiya, S.; Aramaki, Y. *J. Control. Release* **2006,** 111, (3), 325-332.
5. Al-Jamal, W. T.; Al-Jamal, K. T.; Cakebread, A.; Halket, J. M.; Kostarelos, K. *Bioconjugate Chem.* **2009,** 20, (9), 1696-1702.
6. Yeeprae, W.; Kawakami, S.; Suzuki, S.; Yamashita, F.; Hashida, M. *Pharmazie* **2006,** 61, (2), 102-105.
7. Abu Lila, A. S.; Kizuki, S.; Doi, Y.; Suzuki, T.; Ishida, T.; Kiwada, H. *J. Control. Release* **2009,** 137, (1), 8-14.
8. Yaroslavov, A. A.; Rakhnyanskaya, A. A.; Yaroslavova, E. G.; Efimova, A. A.; Menger, F. M. *Adv. Colloid Interfac.* **2008,** 142, (1-2), 43-52.
9. Obata, Y.; Suzuki, D.; Takeoka, S. *Bioconjugate Chem.* **2008,** 19, (5), 1055-1063.
10. Jordan, R.; West, N.; Ulman, A.; Chou, Y.-M.; Nuyken, O. *Macromolecules* **2001,** 34, (6), 1606-1611.
11. Zhou, Z.; Shen, Y.; Tang, J.; Fan, M.; Van Kirk, E. A.; Murdoch, W. J.; Radosz, M. *Adv. Funct. Mater.* **2009,** 19, (22), 3580-3589.

12. Murthy, N.; Robichaud, J. R.; Tirrell, D. A.; Stayton, P. S.; Hoffman, A. S. *J. Control. Release* **1999,** 61, (1-2), 137-143.
13. Guin, S.; Yao, H.-P.; Wang, M.-H. *Mol. Pharm.* **2010,** 7, (2), 386-397.
14. Jung, S. H.; Jung, S. H.; Seong, H.; Cho, S. H.; Jeong, K.-S.; Shin, B. C. *Int. J. Pharm.* **2009,** 382, (1-2), 254-261.
15. Patil, K. M.; Naik, R. J.; Rajpal; Fernandes, M.; Ganguli, M.; Kumar, V. A. *J. Am. Chem. Soc.* **2012,** 134, (17), 7196-7199.
16. Ruoslahti, E. *Adv. Mater.* **2012,** 24, (28), 3747-3756.
17. Yan, M.; Du, J.; Gu, Z.; Liang, M.; Hu, Y.; Zhang, W.; Priceman, S.; Wu, L.; Zhou, Z. H.; Liu, Z.; Segura, T.; Tang, Y.; Lu, Y. *Nat. Nanotechnol.* **2010,** 5, (1), 48-53.
18. Hoyer, J.; Neundorf, I. *Acc. Chem. Res.* **2012,** 45, (7), 1048-1056.
19. Schwarze, S. R.; Ho, A.; Vocero-Akbani, A.; Dowdy, S. F. *Science* **1999,** 285, (5433), 1569-1572.
20. Sarko, D.; Beijer, B.; Boy, R. G.; Nothelfer, E.-M.; Leotta, K.; Eisenhut, M.; Altmann, A.; Haberkorn, U.; Mier, W. *Mol. Pharm.* **2010,** 7, (6), 2224-2231.
21. van Duijnhoven, S. M. J.; Robillard, M. S.; Nicolay, K.; Grull, H. *J. Nucl. Med.* **2011,** 52, (2), 279-286.
22. Sethuraman, V. A.; Bae, Y. H. *J. Control. Release* **2007,** 118, (2), 216-224.
23. Itaka, K.; Kataoka, K. *Curr. Gene Ther.* **2011,** 11, (6), 457-465.
24. Lee, E. S.; Gao, Z.; Kim, D.; Park, K.; Kwon, I. C.; Bae, Y. H. *J. Control. Release* **2008,** 129, (3), 228-236.
25. Jin, E.; Zhang, B.; Sun, X.; Zhou, Z.; Ma, X.; Sun, Q.; Tang, J.; Shen, Y.; Van Kirk, E.; Murdoch, W. J.; Radosz, M. *J. Am. Chem. Soc.* **2013,** 135, (2), 933-940.
26. Tekade, R. K.; Kumar, P. V.; Jain, N. K. *Chem. Rev.* **2009,** 109, (1), 49-87.
27. Astruc, D.; Boisselier, E.; Ornelas, C. *Chem. Rev.* **2010,** 110, (4), 1857-1959.
28. Jang, W.-D.; Kamruzzaman Selim, K. M.; Lee, C.-H.; Kang, I.-K. *Prog. Polym. Sci.* **2009,** 34, (1), 1-23.
29. Sadekar, S.; Ghandehari, H. *Adv. Drug Deliv. Rev.* **2012,** 64, (6), 571-588.
30. Mishra, V.; Gupta, U.; Jain, N. K. *J. Biomater. Sci., Polym. Ed.* **2009,** 20, (2), 141-166.
31. Malik, N.; Wiwattanapatapee, R.; Klopsch, R.; Lorenz, K.; Frey, H.; Weener, J. W.; Meijer, E. W.; Paulus, W.; Duncan, R. *J. Control. Release* **2000,** 65, (1-2), 133-148.
32. Kitchens, K. M.; El-Sayed, M. E. H.; Ghandehari, H. *Adv. Drug Deliv. Rev.* **2005,** 57, (15), 2163-2176.
33. Padilla De Jesus, O. L.; Ihre, H. R.; Gagne, L.; Frechet, J. M. J.; Szoka, F. C., Jr. *Bioconjugate Chem.* **2002,** 13, (3), 453-461.
34. Feliu, N.; Walter, M. V.; Montanez, M. I.; Kunzmann, A.; Hult, A.; Nystrom, A.; Malkoch, M.; Fadeel, B. *Biomaterials* **2012,** 33, (7), 1970-1981.
35. Lee, C. C.; MacKay, J. A.; Frechet, J. M. J.; Szoka, F. C. *Nat. Biotechnol.* **2005,** 23, (12), 1517-1526.
36. Gillies, E. R.; Dy, E.; Frechet, J. M. J.; Szoka, F. C. *Mol. Pharm.* **2005,** 2, (2), 129-138.
37. Almutairi, A.; Akers, W. J.; Berezin, M. Y.; Achilefu, S.; Frechet, J. M. J. *Mol. Pharm.* **2008,** 5, (6), 1103-1110.
38. Guillaudeu, S. J.; Fox, M. E.; Haidar, Y. M.; Dy, E. E.; Szoka, F. C.; Frechet, J. M. J. *Bioconjugate Chem.* **2008,** 19, (2), 461-469.
39. Ye, M. Z.; Qian, Y.; Shen, Y. Q.; Hu, H. J.; Sui, M. H.; Tang, J. B. *J. Mater. Chem.* **2012,** 22, (29), 14369-14377.
40. Ihre, H.; Hult, A.; Soderlind, E. *J. Am. Chem. Soc.* **1996,** 118, (27), 6388-6395.
41. Ihre, H.; Hult, A.; Frechet, J. M. J.; Gitsov, I. *Macromolecules* **1998,** 31, (13), 4061-4068.
42. Ropponen, J.; Tuuttila, T.; Lahtinen, M.; Nummelin, S.; Rissanen, K. *J. Polym. Sci. Pol. Chem.* **2004,** 42, (22), 5574-5586.
43. Malkoch, M.; Malmstroem, E.; Hult, A. *Macromolecules* **2002,** 35, (22), 8307-8314.
44. Frechet, J. M. J.; Ihre, H.; De Jesus, O. L. P. *J. Am. Chem. Soc.* **2001,** 123, (25), 5908-5917.
45. Parrott, M. C.; Marchington, E. B.; Valliant, J. F.; Adronov, A. *J. Am. Chem. Soc.* **2005,** 127, (34), 12081-12089.
46. Ma, X.; Zhou, Z.; Jin, E.; Sun, Q.; Zhang, B.; Tang, J.; Shen, Y. *Macromolecules* **2013,** 46, (1), 37-42.
47. Ropponen, J.; Nummelin, S.; Rissanen, K. *Org. Lett.* **2004,** 6, (15), 2495-2497.
48. Jin, R.; Dijkstra, P. J.; Feijen, J. *J. Control. Release* **2010,** 148, (1), e41-e43.
49. Dondoni, A.; Marra, A. *Chem. Soc. Rev.* **2012,** 41, (2), 573-586.

50. Wang, N.; Dong, A.; Tang, H.; Van Kirk, E. A.; Johnson, P. A.; Murdoch, W. J.; Radosz, M.; Shen, Y. *Macromol. Biosci.* **2007,** 7, (11), 1187-1198.
51. Lowe, A. B.; Hoyle, C. E.; Bowman, C. N. *J. Mater. Chem.* **2010,** 20, (23), 4745-4750.
52. Syrett, J. A.; Jones, M. W.; Haddleton, D. M. *Chem. Commun. (Camb.)* **2010,** 46, (38), 7181-7183.
53. Ono, Y.; Shikata, T. *J. Am. Chem. Soc.* **2006,** 128, (31), 10030-10031.
54. Wang, C.; Flynn, N. T.; Langer, R. *Adv. Mater.* **2004,** 16, (13), 1074-1079.
55. Lim, J.; Simanek, E. E. *Adv. Drug Deliv. Rev.* **2012,** 64, (9), 826-835.
56. Walter, M. V.; Malkoch, M. *Chem. Soc. Rev.* **2012,** 41, (13), 4593-4609.
57. Menjoge, A. R.; Kannan, R. M.; Tomalia, D. A. *Drug Discov. Today* **2010,** 15, (5-6), 171-185.
58. Wolinsky, J. B.; Grinstaff, M. W. *Adv. Drug Deliv. Rev.* **2008,** 60, (9), 1037-1055.
59. Shen, Y.; Zhuo, Z.; Sui, M.; Tang, J.; Xu, P.; Van Kirk, E. A.; Murdoch, W. J.; Fan, M.; Radosz, M. *Nanomedicine* **2010,** 5, (8), 1205-1217.
60. Ye, L.; Letchford, K.; Heller, M.; Liggins, R.; Guan, D.; Kizhakkedathu, J. N.; Brooks, D. E.; Jackson, J. K.; Burt, H. M. *Biomacromolecules* **2011,** 12, (1), 145-155.
61. Duncan, R.; Izzo, L. *Adv. Drug Deliv. Rev.* **2005,** 57, (15), 2215-2237.
62. Patri, A. K.; Kukowska-Latallo, J. F.; Baker, J. R. *Adv. Drug Deliv. Rev.* **2005,** 57, (15), 2203-2214.
63. Ma, X.; Sun, Q.; Zhou, Z.; Jin, E.; Tang, J.; Van Kirk, E.; Murdoch, W. J.; Shen, Y. *Polym. Chem.* **2013,** 4, (3), 812-819.
64. Tong, R.; Christian, D. A.; Tang, L.; Cabral, H.; Baker, J. R., Jr.; Kataoka, K.; Discher, D. E.; Cheng, J. *Mrs Bull.* **2009,** 34, (6), 422-431.
65. Danhier, F.; Feron, O.; Preat, V. *J. Control. Release* **2010,** 148, (2), 135-146.
66. Barenholz, Y. *J. Control. Release* **2012,** 160, (2), 117-134.
67. Gaucher, G.; Marchessault, R. H.; Leroux, J.C. *J. Control. Release* **2010,** 143, (1), 2-12.
68. Jang, S. H.; Wientjes, M. G.; Lu, D.; Au, J. L. S. *Pharm. Res.* **2003,** 20, (9), 1337-1350.
69. Jain, R. K. *Science* **2005,** 307, (5706), 58-62.
70. Jain, R. K. *Adv. Drug Deliv. Rev.* **2001,** 46, (1-3), 149-168.
71. Choi, J.; Credit, K.; Henderson, K.; Deverkadra, R.; He, Z.; Wiig, H.; Vanpelt, H.; Flessner, M. F. *Clin. Cancer Res.* **2006,** 12, (6), 1906-1912.
72. Boucher, Y.; Baxter, L. T.; Jain, R. K. *Cancer Res.* **1990,** 50, (15), 4478-4484.
73. Heldin, C. H.; Rubin, K.; Pietras, K.; Ostman, A. *Nat. Rev. Cancer* **2004,** 4, (10), 806-813.
74. Cabral, H.; Matsumoto, Y.; Mizuno, K.; Chen, Q.; Murakami, M.; Kimura, M.; Terada, Y.; Kano, M. R.; Miyazono, K.; Uesaka, M.; Nishiyama, N.; Kataoka, K. *Nat. Nanotechnol.* **2011,** 6, (12), 815-823.
75. Jain, R. K. *Cancer Res.* **1990,** 50, (3), S814-S819.
76. Holback, H.; Yeo, Y. *Pharm. Res.* **2011,** 28, (8), 1819-1830.
77. Perrault, S. D.; Walkey, C.; Jennings, T.; Fischer, H. C.; Chan, W. C. W. *Nano Lett.* **2009,** 9, (5), 1909-1915.
78. Li, S.D.; Huang, L. *Mol. Pharm.* **2008,** 5, (4), 496-504.
79. Amrite, A. C.; Edelhauser, H. F.; Singh, S. R.; Kompella, U. B. *Mol. Vis.* **2008,** 14, (19-23).
80. Yang, Z.; Leon, J.; Martin, M.; Harder, J. W.; Zhang, R.; Liang, D.; Lu, W.; Tian, M.; Gelovani, J. G.; Qiao, A.; Li, C. *Nanotechnology* **2009,** 20, (16), 165101.
81. Mishra, S.; Webster, P.; Davis, M. E. *Eur. J. Cell Bio.* **2004,** 83, (3), 97-111.
82. Juweid, M.; Neumann, R.; Paik, C.; Perezbacete, M. J.; Sato, J.; Vanosdol, W.; Weinstein, J. N. *Cancer Res.* **1992,** 52, (19), 5144-5153.
83. Ma, X. P.; Tang, J. B.; Shen, Y. Q.; Fan, M. H.; Tang, H. D.; Radosz, M. *J. Am. Chem. Soc.* **2009,** 131, (41), 14795-14803.
84. Shen, Y.; Ma, X.; Zhang, B.; Zhou, Z.; Sun, Q.; Jin, E.; Sui, M.; Tang, J.; Wang, J.; Fan, M. *Chemistry (Weinheim an der Bergstrasse, Germany)* **2011,** 17, (19), 5319-5326.
85. Hatakeyama, H.; Akita, H.; Harashima, H. *Adv. Drug Deliv. Rev.* **2011,** 63, (3), 152-160.
86. Pasut, G.; Veronese, F. M. *Adv. Drug Deliv. Rev.* **2009,** 61, (13), 1177-1188.
87. Rodrigues, D. G.; Maria, D. A.; Fernandes, D. C.; Valduga, C. J.; Couto, R. D.; Ibanez, O. C. M.; Maranhao, R. C. *Cancer Chemother. Pharmacol.* **2005,** 55, (6), 565-576.
88. Kirby, C.; Clarke, J.; Gregoriadis, G. *Biochem. J.* **1980,** 186, (2), 591-598.

89. Cauda, V.; Schlossbauer, A.; Kecht, J.; Zurner, A.; Bein, T. *J. Am. Chem. Soc.* **2009,** 131, (32), 11361-11370.
90. Diaz-Moscoso, A.; Vercauteren, D.; Rejman, J.; Benito, J. M.; Ortiz Mellet, C.; De Smedt, S. C.; Garcia Fernandez, J. M. *J. Control. Release* **2010,** 143, (3), 318-325.
91. Orlandi, P. A.; Fishman, P. H. *J. Cell Bio.* **1998,** 141, (4), 905-915.
92. Davol, P. A.; Bizuneh, A.; Frackelton, A. R. *Anticancer Res.* **1999,** 19, (3A), 1705-1713.
93. Kono, K.; Igawa, T.; Takagishi, T. *Biochim. Biophys. Acta* **1997,** 1325, (2), 143-154.
94. Struck, D. K.; Hoekstra, D.; Pagano, R. E. *Biochemistry* **1981,** 20, (14), 4093-4099.
95. Moghimi, S. M.; Hunter, A. C.; Murray, J. C. *Pharmacol. Rev.* **2001,** 53, (2), 283-318.
96. Alexis, F.; Pridgen, E.; Molnar, L. K.; Farokhzad, O. C. *Mol. Pharm.* **2008,** 5, (4), 505-515.
97. Yoo, J. W.; Chambers, E.; Mitragotri, S. *Curr. Pharm. Des.* **2010,** 16, (21), 2298-2307.
98. Popović, Z.; Liu, W.; Chauhan, V. P.; Lee, J.; Wong, C.; Greytak, A. B.; Insin, N.; Nocera, D. G.; Fukumura, D.; Jain, R. K.; Bawendi, M. G. *Angew. Chem. Int. Ed.* **2010,** 49, (46), 8649-8652.
99. Zhu, Z.; Xie, C.; Liu, Q.; Zhen, X.; Zheng, X.; Wu, W.; Li, R.; Ding, Y.; Jiang, X.; Liu, B. *Biomaterials* **2011,** 32, (35), 9525-9535.
100. Schadlich, A.; Caysa, H.; Mueller, T.; Tenambergen, F.; Rose, C.; Gopferich, A.; Kuntsche, J.; Mader, K. *Acs Nano* **2011,** 5, (11), 8710-8720.
101. Geng, Y.; Dalhaimer, P.; Cai, S. S.; Tsai, R.; Tewari, M.; Minko, T.; Discher, D. E. *Nat. Nanotechnol.* **2007,** 2, (4), 249-255.
102. Christian, D. A.; Cai, S. S.; Garbuzenko, O. B.; Harada, T.; Zajac, A. L.; Minko, T.; Discher, D. E. *Mol. Pharm.* **2009,** 6, (5), 1343-1352.
103. Loverde, S. M.; Klein, M. L.; Discher, D. E. *Adv. Mater.* **2011,** 24, (28), 3823-3830.
104. Fox, M. E.; Szoka, F. C.; Fréchet, J. M. J. *Acc. Chem. Res.* **2009,** 42, (8), 1141-1151.
105. Prencipe, G.; Tabakman, S. M.; Welsher, K.; Liu, Z.; Goodwin, A. P.; Zhang, L.; Henry, J.; Dai, H. J. *J. Am. Chem. Soc.* **2009,** 131, (13), 4783-4787.
106. Venkataraman, S.; Hedrick, J. L.; Ong, Z. Y.; Yang, C.; Ee, P. L. R.; Hammond, P. T.; Yang, Y. Y. *Adv. Drug Deliv. Rev.* **2011,** 63, (14-15), 1228-1246.
107. Giri, S.; Trewyn, B. G.; Stellmaker, M. P.; Lin, V. S. Y. *Angew. Chem. Int. Ed.* **2005,** 44, (32), 5038-5044.
108. Wijaya, A.; Schaffer, S. B.; Pallares, I. G.; Hamad-Schifferli, K. *Acs Nano* **2009,** 3, (1), 80-86.
109. Chauhan, V. P.; Popovic, Z.; Chen, O.; Cui, J.; Fukumura, D.; Bawendi, M. G.; Jain, R. K. *Angew. Chem. Int. Ed* **2011,** 50, (48), 11417-20.
110. Gratton, S. E. A.; Ropp, P. A.; Pohlhaus, P. D.; Luft, J. C.; Madden, V. J.; Napier, M. E.; DeSimone, J. M. *Proc. Natl. Acad. Sci. USA* **2008,** 105, (33), 11613-11618.
111. Petros, R. A.; DeSimone, J. M. *Nat. Rev. Drug Discov.* **2010,** 9, (8), 615-627.
112. Meng, H.; Yang, S.; Li, Z.; Xia, T.; Chen, J.; Ji, Z.; Zhang, H.; Wang, X.; Lin, S.; Huang, C.; Zhou, Z. H.; Zink, J. I.; Nel, A. E. *Acs Nano* **2011,** 5, (6), 4434-4447.
113. Takeoka, S.; Mori, K.; Ohkawa, H.; Sou, K.; Tsuchida, E. *J. Am. Chem. Soc.* **2000,** 122, (33), 7927-7935.
114. Pati, D.; Kalva, N.; Das, S.; Kumaraswamy, G.; Sen Gupta, S.; Ambade, A. V. *J. Am. Chem. Soc.* **2012,** 134, (18), 7796-802.
115. Fox, M. E.; Guillaudeu, S.; Frechet, J. M. J.; Jerger, K.; Macaraeg, N.; Szoka, F. C. *Mol. Pharm.* **2009,** 6, (5), 1562-1572.
116. O'Brien, M. E. R.; Wigler, N.; Inbar, M.; Rosso, R.; Grischke, E.; Santoro, A.; Catane, R.; Kieback, D. G.; Tomczak, P.; Ackland, S. P.; Orlandi, F.; Mellars, L.; Alland, L.; Tendler, C.; Grp, C. B. C. S. *Ann. Oncol.* **2004,** 15, (3), 440-449.
117. Gradishar, W. J.; Tjulandin, S.; Davidson, N.; Shaw, H.; Desai, N.; Bhar, P.; Hawkins, M.; O'Shaughnessy, J. *J. Clin. Oncol.* **2005,** 23, (31), 7794-7803.
118. Sun, Q.; Radosz, M.; Shen, Y. *J. Control.Release* **2012,** 164, (2), 156-169.

Key Research Accomplishments

1. We prepared a negative-to-positive charge-reversal liposome for cancer drug targeted delivery. The charge reversal liposome could be effectively cellular internalized with higher cytotoxicity to cancer cells, showing a great promise for *in vivo* administrations.

2. Using TAT as an example, we demonstrated an efficient molecular modification approach that involves reversible blocking/activation of cationic CPPs. The amidized CPPs are very stable and have completely inhibited nonspecific interactions in the blood compartment. Thus, coupled with tissue-specific targeting groups, this approach may greatly widen the door for in vivo applications of CPPs.

3. We developed an efficient synthesis of monodispersed bis-MPA polyester dendrimers using thiol−acrylate reaction and the traditional esterification reaction under mild conditions. The simple synthesis and purification make the dendrimer synthesis straight forward for large-scale production.

4. We developed a convenient synthesis of interior-and-peripheral-bifunctionalized dendritic polymers. These bifunctional dendritic polymers are nontoxic and biodegradable, offering a versatile platform for various biomedical applications.

5. We developed a liposomal dendrimer nanoassembly (*DLC-PEG*) and demonstrated it can improve tumor accumulation, penetration, and cellular uptake. The “cluster bomb” concept may be a very promising approach uniting the needed properties for high chemotherapeutic efficacy.

6. We demonstrated a facile approach to fabricate polymer-drug conjugate nanorods for cancer-drug delivery. The nanorods with medium lengths (<500 nm) also had a much better stealth property and thus a much longer blood circulation time than the nanospheres.

Reportable Outcomes

1. Xinpeng Ma, Zhuxian Zhou, Bo Zhang, Erlei Jin, Qihang Sun, Jianbin Tang, Youqing Shen, Edward Van Kirk, William J. Murdoch, Maciej Radosz. Charge-Reversal Liposomes for Cancer Nuclear Targeted Drug Delivery. Manuscript to be submitted.
2. Erlei Jin, Bo Zhang, Xuanrong Sun, Zhuxian Zhou, Xinpeng Ma, Qihang Sun, Jianbin Tang, Youqing Shen, Edward Van Kirk, William J. Murdoch, Maciej Radosz. Acid-Active Cell-Penetrating Peptides for in Vivo Tumor-Targeted Drug Delivery. Journal of the American Chemical Society, 2013, 135, 933.
3. Xinpeng Ma, Zhuxian Zhou, Erlei Jin, Qihang Sun, Bo Zhang, Jianbin Tang, Youqing Shen. Facile Synthesis of Polyester Dendrimers as Drug Delivery Carriers. Macromolecules, 2013, 46, 37.
4. Xinpeng Ma, Qihang Sun, Zhuxian Zhou, Erlei Jin, Jianbin Tang, Edward Van Kirk, William J. Murdoch, Youqing Shen. Synthesis of Degradable Bifunctional Dendritic Polymers as Versatile Drug Carriers. Polymer Chemistry, 2013, 4, 812.
5. Qihang Sun, Xinpeng Ma, Zhuxian Zhou, Erlei Jin, Bo Zhang, Youqing Shen, Edward Van Kirk, William J. Murdoch, Joseph R. Lott, Timothy P. Lodge, Maciej Radosz. Lipid/Dendrimer Nanoassembly as “Cluster Bomb” for Cascade Tumor Penetration. To be submitted to Nature Materials.
6. Zhuxian Zhou, Xinpeng Ma, Erlei Jin, Jianbin Tang, Youqing Shen, Edward Van Kirk, William J. Murdoch, Maciej Radosz. Linear-Dendritic Drug Conjugates Forming Long Circulating Nanorods for Cancer Drug Delivery. Biomaterials, 2013, 34, 5722.
7. Qihang Sun, Maciej Radosz, Youqing Shen. Challenges in design of translational nanocarriers. Journal of Controlled Release, 2012, 164, 156.